

An innovative kinetic model allowing insight in the moderate temperature chemical vapor deposition of silicon oxynitride films from tris(dimethylsilyl)amine

Konstantina Christina Topka, Hugues Vergnes, Tryfon Tsiros, Paris Papavasileiou, Laura Decosterd, Babacar Diallo, François Senocq, Diane Samelor, Nadia Pellerin, Marie-Joëlle Menu, et al.

▶ **To cite this version:**

Konstantina Christina Topka, Hugues Vergnes, Tryfon Tsiros, Paris Papavasileiou, Laura Decosterd, et al.. An innovative kinetic model allowing insight in the moderate temperature chemical vapor deposition of silicon oxynitride films from tris(dimethylsilyl)amine. Chemical Engineering Journal, 2021, 431, pp.133350. 10.1016/j.cej.2021.133350 . hal-03514135

HAL Id: hal-03514135
https://cnrs.hal.science/hal-03514135

Submitted on 18 Jan 2022

HAL is a multi-disciplinary open access archive for the deposit and dissemination of scientific research documents, whether they are published or not. The documents may come from teaching and research institutions in France or abroad, or from public or private research centers.

L'archive ouverte pluridisciplinaire **HAL**, est destinée au dépôt et à la diffusion de documents scientifiques de niveau recherche, publiés ou non, émanant des établissements d'enseignement et de recherche français ou étrangers, des laboratoires publics ou privés.

Chemical Engineering Journal 431 (2022) 133350

An innovative kinetic model allowing insight in the moderate temperature chemical vapor deposition of silicon oxynitride films from tris(dimethylsilyl)amine

Konstantina Christina Topka [a, b], Hugues Vergnes [a],
Tryfon Tsiros [a], Paris Papavasileiou [b], Laura Decosterd [b], Babacar Diallo [c], François Senocq [b], Diane Samelor [b],
Nadia Pellerin [c], Marie-Joëlle Menu [b], Constantin Vahlas [b], Brigitte Caussat [a*]

[a] Laboratoire de Génie Chimique (LGC), Université de Toulouse, CNRS, Toulouse, France

[b] Centre Interuniversitaire de Recherche et d'Ingénierie des Matériaux (CIRIMAT), Université de Toulouse, CNRS, Toulouse, France

[c] Conditions Extrêmes et Matériaux : Haute Température et Irradiation (CEMHTI) UPR 3079, Université d'Orléans, CNRS, Orléans, France

*Corresponding author: brigitte.caussat@ensiacet.fr
LGC, Université de Toulouse, CNRS, Toulouse, France

Abstract

An apparent kinetic model is developed for a novel chemical vapor deposition (CVD) process of silicon oxynitride (SiO_xN_y) films from tris(dimethylsilyl)amine (TDMSA) and O_2, operating at moderate temperature (600-650°C) and at atmospheric pressure. The definition of reaction pathways and the extraction of kinetic information is based on recently reported results of the gas phase composition, complemented by solid phase characteristics obtained by spectroscopic ellipsometry (SE) and ion beam analyses (IBA). Incorporation of carbon (up to 20 at.%) is considered alongside nitrogen (up to 25 at.%) for variable O_2 flow rates (0.3-1.2 sccm). This combined gas- and solid-phase analysis is utilized to identify the main gaseous species and provide insight into the deposition mechanism. A silicon- and a nitrogen-centered radical intermediates are considered as the primary species of the mechanism, based on evidence from gas phase characterizations. A third, fictitious nitrogen-containing molecule is also conceptualized to account for carbon incorporation. Eight chemical reactions are defined alongside their respective kinetic parameters and are implemented in the ANSYS® FLUENT® computational fluid dynamics (CFD) code. Upon validation, the model allows for the successful

prediction of local deposition rates and SiO_xN_y film composition containing non-negligible carbon, marking it as the first kinetic model able to represent the main chemical mechanisms involved in the CVD of a four-component material. The reported combined approach could be applied to other existing or new CVD chemistries forming multi-component thin films, favoring their implementation in original applications.

Keywords: Chemical vapor deposition, Silicon oxynitride, Silanamine precursor, Computational fluid dynamics, Kinetic model, Experimental validation.

1. Introduction

Silicon oxynitride (SiO_xN_y) thin films exhibit attractive physical properties, which can be tailored between those of SiO_2 and Si_3N_4 by modulating their nitrogen content. Their thermal and chemical stability, hardness and anti-corrosion properties are upgraded in comparison to those of pure silica, due to the partial replacement of O^{2-} anions by higher coordinated N^{3-} ones [1-3]. Their intrinsic mechanical stress is concomitantly reduced in comparison to the more rigid Si_3N_4 films [4]. For these reasons, silicon oxynitride thin films have found numerous applications in the fields of solar cells, ion sensing, semiconductors and packaging [1, 5-9].

Despite this wide application potential, further implementation of SiO_xN_y films requires solutions to two major constraints: the deposition at moderate temperature to treat a variety of thermally sensitive parts on one hand, and the homogeneous-in-composition and conformal coverage of surfaces with non-line-of-sight geometries on the other. Chemical vapor deposition (CVD) presents a suitable option for the accomplishment of the above, even on substrates with high 3D complexity, explaining why it has been historically implemented in critical processes relating to silicon and silicon-based materials [10, 11]. Existing thermal CVD routes that form SiO_xN_y thin films classically involve silane or chlorosilane precursors, often mixed with NH_3 and N_2O. These processes operate at deposition temperatures higher than 700°C [12-14], which drastically limits their application on heat sensitive substrates.

A solution to simultaneously address these constraints is tuning an appropriate process based on an innovative chemical pathway. The present work details such a solution with atmospheric pressure CVD, using mixtures of tris(dimethylsilyl)amine ($N(SiHMe_2)_3$, TDMSA) and O_2. On one hand, the silanamine TDMSA precursor contains three nitrogen atoms and does not require additional nitrogen-containing reagents like NH_3 for the deposition of SiO_xN_y films. On the other, the choice of O_2 as the oxidant is based on its lower oxidation potential compared to O_3, thus avoiding the complete oxidation of the Si-N bonds in the precursor. Moreover, the use of TDMSA allows for decreasing the minimum-required deposition temperature by thermal CVD towards the 600-650°C range, attributed to the presence of Si-H bonds in its chemical structure, which enhances precursor reactivity [15, 16]. However, the deposition mechanism is chemically complex and the composition and short-range order structure of the resulting SiO_xN_y films strongly depend on the starting precursor chemistry. Indeed, many among the numerous intermediates and by-products formed in the gas phase influence the composition and properties of the resulting SiO_xN_y film, oftentimes introducing carbon therein. An efficient way to assist the tuning of such a novel process is its simulation using a computational fluid dynamics (CFD)

code associated with an apparent kinetic model, in other words, a model describing a complex deposition mechanism in a simplified manner, based on consideration of the most representative chemical reactions involved. Valuable information can indeed be obtained through this approach: local gas flow, temperature, species distribution profiles, local deposition rates and film composition profiles on the substrates at the reactor scale, inter alia. Moreover, once developed and validated, the simulation outcome can serve as an efficient tool for optimizing the deposition process on complex-in-shape, large, and/or multi-part substrates [17].

To this extent, it is necessary to rely on a robust and representative kinetic model. In the past decades, this has been achieved for the CVD of the binary silicon dioxide (SiO_2) and silicon nitride (Si_3N_4) systems. Numerous chemical pathways and kinetic models have been reported for the deposition of SiO_2 from SiH_4 [18], chlorosilanes [19, 20] and alkoxysilane precursors such as tetraethylorthosilicate (TEOS) [21-23]. For Si_3N_4, mechanisms have been proposed for its deposition from SiH_4 and NH_3 [24-26]. However, the complexity of the quaternary carbonated SiO_xN_y system, combined with the involvement of a silanamine precursor, goes beyond the existing models for binary materials. Combined with the requirements for deposition at moderate temperature alongside the inadvertent incorporation of carbon, makes that such a model has not been reported yet to this date. Formulation of a comprehensive deposition mechanism from a complex chemistry, even in a simplified form, is a challenge, making the local probing of the gaseous reactive species and produced by-products essential.

In a non-intrusive manner yet still sensitive enough to identify short-lived species, an innovative methodology, implemented recently by the authors for the on-line characterization of the gas phase and the definition of reaction pathways during the atmospheric pressure CVD of carbonated SiO_xN_y from TDMSA and O_2 [15], is exploited. Detection and identification of gaseous radical species and stable by-products alike in the effluent gases of the CVD reactor was done by combination of gas chromatography - mass spectrometry (GC-MS), nuclear magnetic resonance (NMR) and electron spin resonance (ESR). Through quantitative and qualitative GC-MS analysis, the TDMSA precursor decomposition was investigated and the various homolytic dissociation pathways that give rise to a large number of gaseous by-products were underlined. These analyses were accompanied by characterization of the SiO_xN_y film composition. In particular, an increase of the O_2 supply led to the production of several siloxane products in the gas phase, which was reflected in a more pronounced oxide character of the films. In contrast, nitrogen-containing gaseous by-products were detected by reducing the O_2 flow rate, resulting in films with higher nitrogen content. Consideration of the decomposition

pathways and produced molecules highlights a list of potential reactions involved in the solid film formation. The results accrued through this combined analysis provide precise information on this complex deposition mechanism.

The present work utilizes these results to develop a simplified, though representative, apparent chemical model for the deposition of carbonated SiO_xN_y films, alongside the extraction of associated reaction kinetics, adapted to the particular reactor configuration and operating range (600-650°C). The strategy behind the development of this novel chemical model from scratch will follow the idea of starting from a basic system and enriching it progressively, through systematic comparison between the simulated and the experimental results at each step. The addition of new chemical species and reactions to the model will be motivated through inspection of the results obtained from the combined gas and solid phase analyses reported previously [15]. As a result, initial kinetic constants will progressively undergo further refinements whenever the chemical model is enriched. Implementation within the simulation environment is carried out in the above-described iterative process, until a satisfactory agreement with the experimental results is reached, all the while considering the compromise between model complexity, numerical load, computational time and accuracy.

2. Materials and methods

2.1. On purpose configuration of the CVD reactor and deposition conditions

Deposition of SiO_xN_y films was performed in a tubular, horizontal hot-wall reactor presented schematically in Fig. 1 (a). The reactor consisted of a fused silica tube with an inner diameter of 4.6 cm and a length of 70.0 cm, heated by a semi-transparent furnace (Trans Temp, Thermcraft Inc.) that allows for visual observation of the samples during deposition. The temperature profile at the reactor walls was established by measuring the temperature every 2.0 cm along the tube under a N_2 gas flow of 4030 standard cubic centimeters per minute (sccm) - i.e. the nominal flow rate of the gas phase in deposition conditions - using a type-K thermocouple with an accuracy of ±2°C. The reaction chamber featured a thermal gradient between 0.0 and 36.0 cm, followed by an isothermal region spanning from 36.0 to 50.0 cm. Deposition experiments were performed at set point temperatures (SPT) of 625°C and 650°C, defined as the temperature measured at 36.0 cm from the inlet.

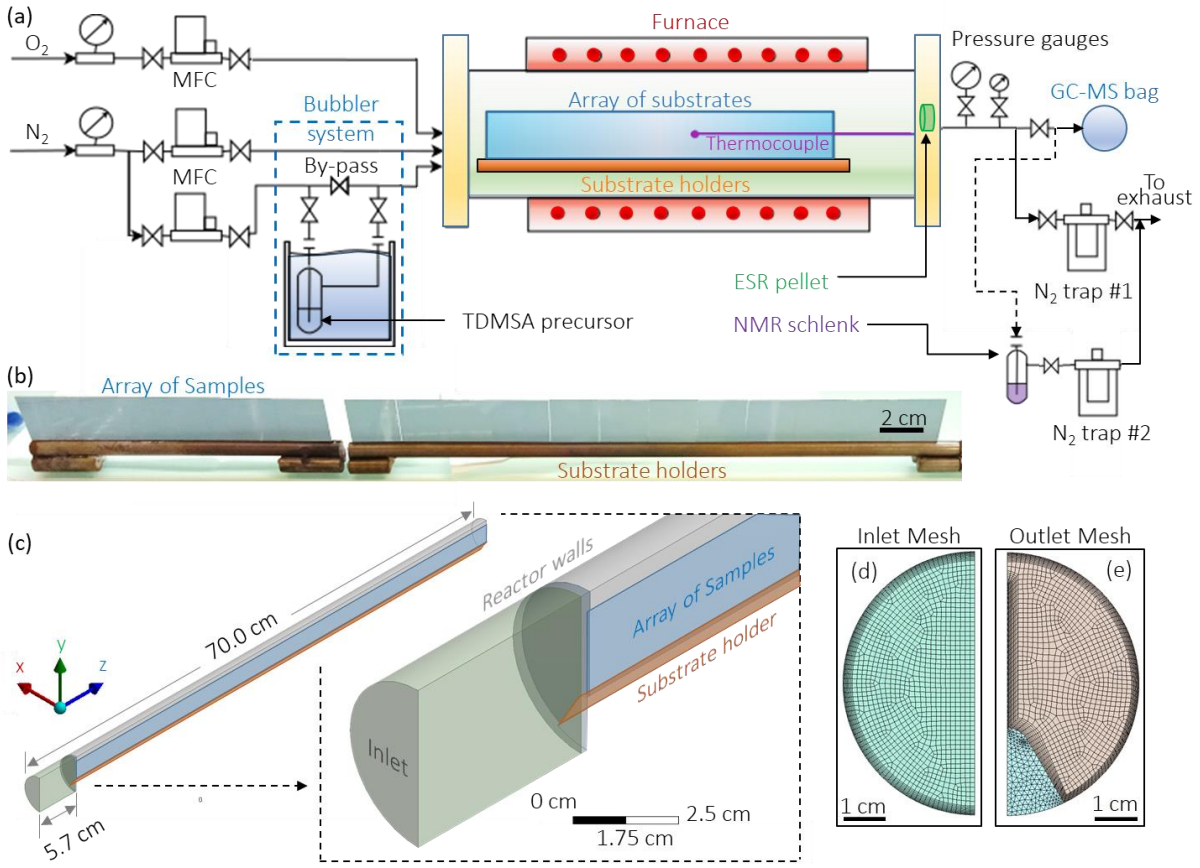


Fig. 1. Schematic representation of the horizontal CVD reactor (a), photograph of the arrangement of Si samples within the stainless steel substrate-holders (b), isometric view of the 3D geometry of the tubular CVD reactor with inset close-up of the inlet region (c), and view of the inlet at 0 cm (d) and outlet at 70 cm (e) after meshing.

280 μm thick monocrystalline silicon (100) wafers (Neyco) were cut in 3.2×2.4 cm^2 rectangles and used as substrates, supported in a vertical array by two home-made, tubular, stainless steel substrate-holders, as illustrated in the photograph in Fig. 1 (b), covering the 5.7-50.0 cm region of the reactor [27]. A total of 18 Si coupons were utilized for each run. No samples were placed beyond 50.0 cm. Similar to our previous works [23, 27], this configuration was chosen deliberately, since the simultaneous processing of thin films within the non-isothermal and isothermal zones can assist in obtaining complementary mechanistic and kinetic information. Before being inserted into the reactor, the Si substrates were degreased in a succession of three ultrasound bath steps described elsewhere [27].

The CVD reactor inlet was connected to three gas lines. A N_2 (99.9999%, Messer) dilution line, heated at approximately 100°C, provided 3980 sccm N_2. A N_2 carrier gas line

bubbled 49 sccm of N_2 gas through a bubbler system containing TDMSA (95 %, ABCR) and transported 2 sccm of the precursor vapors towards the reactor. The bubbler was heated at 80±0.1°C, while the N_2 carrier gas line was kept at approximately 95°C to avoid recondensation of the precursor vapors. An O_2 (99.9995%, Messer) line provided 0.3, 0.6 or 1.2 sccm of O_2 gas. Mass flow controllers were used to monitor all gas flow rates. The gas lines were kept separated, with their contents mixing only after reaching the inlet of the reactor (Fig. 1 (a)). The reactor base and operating pressures were monitored using Pirani (MKS MicroPirani Transducer Series 925C) and Baratron (MKS Baratron Type 627) gauges, respectively, positioned downstream of the deposition zone and upstream of liquid nitrogen traps. The operating pressure was fixed at 97.3 kPa (730 Torr) for all runs. Four runs were performed in total: three runs at SPT 650°C with O_2 flow rates of 0.3, 0.6 and 1.2 sccm and one run at SPT 625°C, with the O_2 flow rate fixed at 0.6 sccm. The deposition time was adjusted to 150 min (for 0.6 and 1.2 sccm O_2) and 225 min (for 0.3 sccm O_2), aiming to produce films with thickness between 100 and 150 nm for subsequent ion beam analysis (IBA). Details on the on-line characterization of the gas phase analyses shown in Fig. 1 (a) are reported elsewhere [15].

2.2. SiO_xN_y film characterization

Local thickness and composition profiles were measured by spectroscopic ellipsometry (SE) using a Semilab SE-2000 ellipsometer operating in the 250-1000 nm wavelength range. The incidence angle was kept constant at 70°. Each sample was probed on five locations along the vertical center line, each 5 mm apart, starting 2 mm below the top edge of each sample. The probing positions are illustrated in Fig. S1 of *Supplementary Material*. The SE data were fitted in the 250-1000 nm range using the Semilab SEA software. The average thickness, average deposition rate (DR) and average film composition were calculated from the average of these five points. Using a Bruggeman Effective Medium Approximation (BEMA) model, a successful fit of the SE spectra was obtained for all films, considered as a mixture of three components that globally result in a homogeneous carbonated SiO_xN_y film. The utilized components were SiO_2, Si_3N_4 and a carbon-containing component. The definition of the latter was based on FT-IR analysis (Fig. S2 of *Supplementary Material*) that revealed the incorporation of $Si\text{-}CH_3$ moieties in all SiO_xN_y films, originating from an incomplete decomposition of the TDMSA precursor. It is noted that only a minimal incorporation of carbon in a $Si\text{-}C_4$ carbidic bonding state was confirmed by X-ray photoelectron spectroscopy (Fig. S3 of *Supplementary Material*). The presence of carbon can thus not be represented through the

use of the SiC SE component and must instead be represented by an organic carbon component. Since the SE database does not include any $–CH_3$ species, an amorphous-C component was utilized instead to represent the incorporation of organic carbon in the films. Fitting of the acquired SE spectra using the BEMA model gave information about the total film thickness and the volumetric fraction of each component. The latter was used to extract information regarding the film composition. For a three-component model, i.e. n=3, the following equation was used to calculate the molar fraction x_i (mol. %) of component *i*:

$$x_i = \frac{f_i \frac{\rho_i}{Mr_i}}{\sum_{i=1}^{i=n} \left(f_i \frac{\rho_i}{Mr_i}\right)} \quad \text{Eq. (1)}$$

Where f_i is the volumetric fraction (vol. %) of component *i* as calculated by SE, Mr_i its molecular weight (g.mol^{-1}) and ρ_i its density (g.cm^{-3}). After using Eq. (1) to calculate the molar fraction of each component, the atomic percentage of each element is then calculated. For SiO_2 and Si_3N_4, the density and molecular weight values were set equal to 2.65 g.cm^{-3} and 60.08 g.mol^{-1}, and 3.17 g.cm^{-3} and 140.28 g.mol^{-1}, respectively. For amorphous carbon, an atomic weight of 12.00 g.mol^{-1} was assigned. However, assignment of a density value to this component is not straightforward. For this reason, accurate composition results in terms of Si, O, N, C and H contents were obtained by coupling Rutherford Backscattering Spectroscopy (RBS), Nuclear Reaction Analysis (NRA) and Elastic Recoil Detection Analysis (ERDA) (shortly referred to as ion beam analyses, IBA), performed at the Pelletron facility of CEMHTI in Orléans, France. Details on these characterizations have been reported elsewhere [15, 28]. For these analyses, the middle of the sample positioned at 38.4 cm from the inlet was probed for all runs. These results were used as a calibration method in order to define the density value of the SE carbon component, for which the composition given by SE is close to that measured by IBA. This density value of the amorphous-C SE component was calculated as 0.69 g.cm^{-3}. A sample placed at 43.2 cm from the inlet was also analyzed to confirm and validate the composition calculated by the SE model. Upon validation, the obtained SE thickness and composition data for each experimental run were systematically used to evaluate the agreement between the experimental results and those obtained from the CFD simulations, as well as extract kinetic parameters for the solid phase reactions.

2.3. Computational details

The reaction chamber geometry, consisting of the quartz tube, substrate holders and array of substrates, was replicated in a 3D spatial domain as illustrated in Fig. 1 (c) and is described in more detail elsewhere [27]. Only half of the reactor is considered, due to mirroring symmetry along the YZ plane. It is noted that the vertical YZ plane passing through the samples is used for plotting the reaction rates, while the horizontal XZ plane passing through the center of the reactor is used for plotting the temperature, velocity and species distribution. The spatial domain was discretized in 241,780 hexahedral and tetrahedral cells. A view of the reactor from the inlet and the outlet sides after meshing is shown in Fig. 1 (d) and (e).

A CFD model considering gas phase and surface chemical reactions was developed to represent the reactive transport phenomena and to simulate local DR profiles and local composition of the films. The local gas flow and temperature profiles were calculated by solving the mass and momentum conservation and thermal energy balance equations in each elementary discretized volume. The local distribution of species mass fractions and local DR were calculated after considering the kinetic data of the homogeneous and heterogeneous reactions into the species conservation equations. The numerical simulations were run using ANSYS® FLUENT® 18.2, with a cell-centered finite volume scheme and second-order spatial accuracy. The numerical complexity was simplified by assuming ideal gases, steady state regime, laminar and incompressible gas flow (Reynolds number lower than 1,000 and Mach number lower than 0.04 in the reactive zone) and by neglecting the heat of reactions, due to high N_2 dilution.

The physical properties and Lennard Jones (L-J) parameters of O_2, N_2 and H_2O were taken from the FLUENT® database. Because of the lack of data in the literature, the L-J parameters of the remaining species were assumed equal to those of molecules with similar chemical structure. The L-J parameters of silanone and the silanimine-type intermediate (denoted N_INT2 and explained later) were set equal to those of silanol (σ=5.25 Å and ε/k=522.7 K) [29]. The L-J parameters of TDMSA and the radicals birthed from its dissociation were equated to those of TEOS (σ=7.03 Å and ε/k=78.6 K) [29]. Lastly, those of the siloxane and silanamine by-products were fixed to the values of octamethylcyclotetrasiloxane (σ = 3.54 Å and ε/k = 1182.43 K) [30]. The physical properties of all gases are calculated locally as a function of the local temperature, pressure and gas composition.

The following boundary conditions were applied:

- A flat mass flow profile was considered for the gas inlet. The total mass flow rate ($kg.s^{-1}$) and all species mass fractions were fixed to the experimental values, with only half of the

total mass flow rate being applied due to consideration of only half of the spatial domain due to mirroring symmetry. The inlet gas temperature was set equal to the temperature of the wall close to the inlet (i.e. 199°C).

- A symmetry boundary condition was applied on the YZ symmetry plane.

- A classical no-slip condition was imposed for the gas velocity on all solid surfaces (reactor walls, substrate holder, substrates). The temperature of these surfaces was set equal to the temperature profile measured experimentally on the reactor walls before deposition. Due to the steep decrease of the temperature at the exhaust, a constant temperature was applied for the last 10.0 cm of the reactor, i.e. between 60.0 and 70.0 cm from the reactor inlet, to avoid backflow and to speed up convergence. Modifying the temperature profile in this region did not impact the results, because samples were placed only between 5.7 and 50.0 cm. The mass flux density of each species was assumed to be equal to the corresponding heterogeneous reaction rates. Deposition is considered to take place on all solid surfaces, namely the reactor walls, the substrate holder and the substrates.

- The reactor exhaust was defined using an outflow boundary condition. The total pressure was fixed at the operating pressure (97.3 kPa). A zero diffusion flux was applied to all other gas phase variables at the exit.

The chemical reaction rates were implemented into FLUENT® in the form of an Arrhenius type expression:

$$R_r = A_{0,r}\, exp^{\left(-\frac{E_{a,r}}{R\,T}\right)} \prod_{i=1}^{i=n} [M_i]^{a_i} \qquad \text{Eq. (2)}$$

For surface reaction rates, R_r (kmol.m^{-2}.s^{-1}) stands for the rate of reaction r, $A_{0,r}$ (kmol.m^{-2}.s^{-1}.Pa^{-n}) is the pre-exponential factor of reaction r, $E_{a,r}$ (kJ.mol^{-1}) is the activation energy of reaction r, T (K) is the local temperature at the surface where reaction r occurs, n is the number of involved species, $[M_i]$ (kmol.m^{-3}) is the concentration of the species i and a_i is the partial order exponent of the species i. For the homogeneous chemical reactions, R_r is expressed in kmol.m^{-3}.s^{-1} and $A_{0,r}$ in kmol.m^{-3}.s^{-1}.Pa^{-n}, whereas T (K) is the temperature of the gas phase.

3. Experimental results

3.1. Influence of the O_2 flow rate

Fig. 2 presents the axial evolution of the average DR (Fig. 2 (a)) and the average film atomic content in O, Si, N and C (Fig. 2 (b) to (d)) as deduced from SE after calibration using IBA, for the three runs performed at SPT 650°C with variable O_2 flow rates. The thermal profile along the reactor for this SPT is also included in the secondary y-axis of all graphs. Under these conditions, the temperature in the first 0.07 m of the reactor remains low, i.e. between 199 and 226°C. After 0.07 m, it rapidly increases to reach the target SPT at 0.36 m, remaining constant at 650°C up to 0.50 m from the inlet.

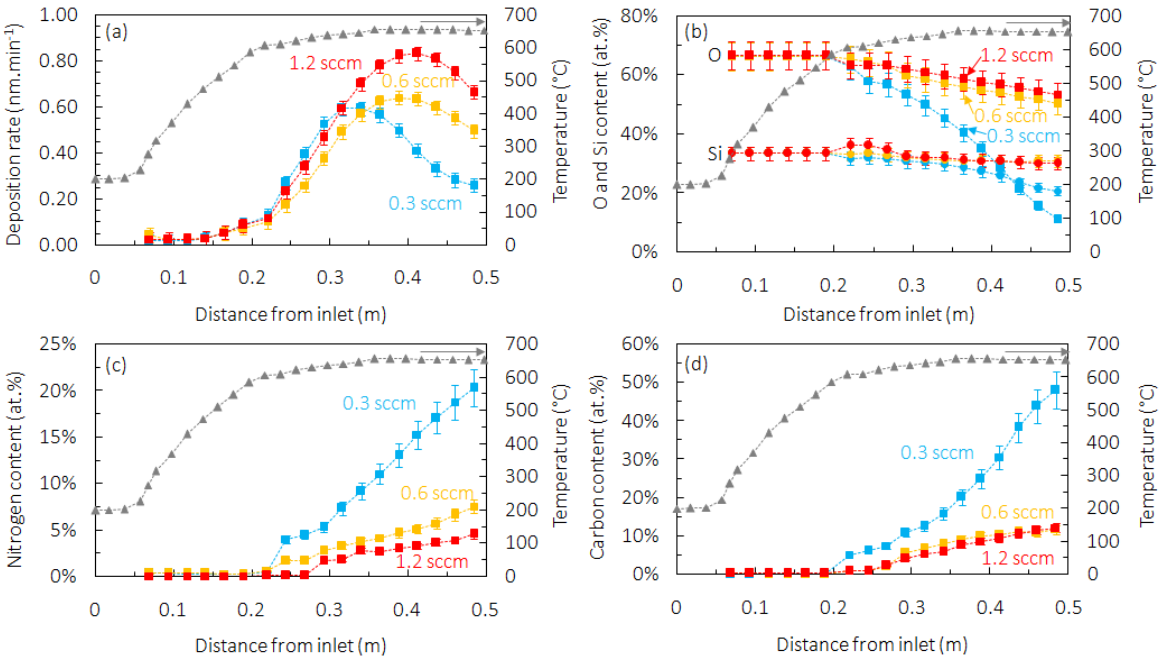


Fig. 2. Influence of the O_2 flow rate on the average DR (a), film oxygen (squares) and silicon (circles) (b) nitrogen (c) and carbon (d) content for runs performed at SPT 650°C.

Fig. 2 (a) reveals that for SPT 650°C, deposition is initiated at ca. 0.19 m for all tested O_2 flow rates, corresponding to a local temperature of 585°C. It is noted that preliminary experiments were done at lower SPTs, namely 550°C and 580°C, and yielded no observable film deposition, in agreement with the initiation of film formation beyond 585°C. Overall, the DR increases with the temperature, illustrating the thermal dependence of the SiO_xN_y deposition process, coherent with the thermal decomposition of TDMSA [15]. Another observation in Fig. 2 (a) is that the presence of O_2 in the gas phase promotes the DR: a maximum DR of 0.57 $nm.min^{-1}$ is measured for 0.3 sccm O_2, increasing to 0.83 $nm.min^{-1}$ for

1.2 sccm O_2. Beyond the maximum DR, deposition decreases as a result of a depletion effect of O_2 or oxygen-containing species that participate in film formation. As such, all DR profiles present a bell shape. Moreover, for higher O_2 supply, the maximum DR value shifts towards the outlet of the reactor, e.g. it is observed at around 0.34 m for 0.3 sccm O_2 and at around 0.41 m for 1.2 sccm O_2. This behavior is linked to the higher O_2 concentration available at 1.2 sccm, which continues promoting any gas phase and/or surface reactions over an extended region.

Fig. 2 (b) presents the O and Si contents incorporated in the films for the three experimental runs at SPT 650°C, as calculated by SE. It is observed that the higher the O_2 supply at the inlet, the higher the oxygen content of the deposited SiO_xN_y material. The depletion effect of O_2 or any film-forming oxygen-containing species is well visible when inspecting the O content for 0.3 sccm O_2. As a result of its lower supply, the amount of oxygen incorporated in the films of this run decreases more abruptly compared to 0.6 and 1.2 sccm O_2. The silicon content is observed to remain fairly constant within a range of 30 to 35 at.% for 0.6 and 1.2 sccm O_2. Decreasing the O_2 supply to 0.3 sccm however results in a Si profile with a negative slope, indicating the increasing incorporation of other elements, namely N and C.

The effect of the O_2 flow rate on the nitrogen content of the films is illustrated in Fig. 2 (c). Overall, nitrogen incorporation is observed for all experiments. It is recalled that other than TDMSA, no additional N-providing reagent, such as NH_3, was utilized. Thus, it is safe to conclude that the incorporated nitrogen originates from the silanamine precursor itself. The N content increases continuously along the length of the reactor, very likely linked to the heating of the gas phase, i.e. production of N-containing species, and solid surfaces, i.e. activation of heterogeneous reactions in which N-containing species are participating. The maximum N content is observed on the last sample of the array. A competitive behavior of O and N incorporation seems to exist, with high values of up to 20.3 at.% N noted for 0.3 sccm O_2, dropping progressively to a maximum of 7.5 at.% and 4.5 at.% N for 0.6 and 1.2 sccm O_2, respectively. Preliminary experiments using 2 sccm O_2 in the same conditions decreased the nitrogen content below 2 at.%, even with the addition of a supplementary nitrogen source, NH_3. For that reason, O_2 supply was defined as 1.2 sccm maximum, in order to retain sufficient nitrogen incorporation in the films.

The evolution of the carbon content is shown in Fig. 2 (d). Similar trends to nitrogen are noted. A maximum C content of 48.0 at.% is observed for 0.3 sccm O_2, decreasing to 12.0 at.% when 1.2 sccm O_2 is used. Overall, the higher the supplied O_2 flow rate, the lower

the carbon incorporation in the films. The results are in agreement with the well-known $–CH_3$ cleaving effect of O_2 in CVD processes using silazane precursors [31-33].

3.2. Influence of the set point temperature

Since notable DR is observed only beyond 585°C (Fig. 2 (a)), deposition at SPT 625°C was studied under the same flow conditions and with the O_2 supply fixed at 0.6 sccm. Fig. 3 summarizes the obtained results for SPT 650°C and 625°C, alongside their corresponding thermal profiles. Inspecting Fig. 3 (a), the DR values for any given position in the reactor are systematically higher at the higher SPT. Maximum DRs of 0.39 $nm.min^{-1}$ and 0.64 $nm.min^{-1}$ are observed for SPT 625°C and 650°C, respectively. The results indicate a strong thermal dependency of the deposition process. The higher deposition rate at the higher SPT could potentially be the result of a surface reaction limited regime. In an alternative case, a transport-limited regime could be responsible, under the condition that the homogeneous reactions that birth the film-forming species are activated and promoted within this temperature range.

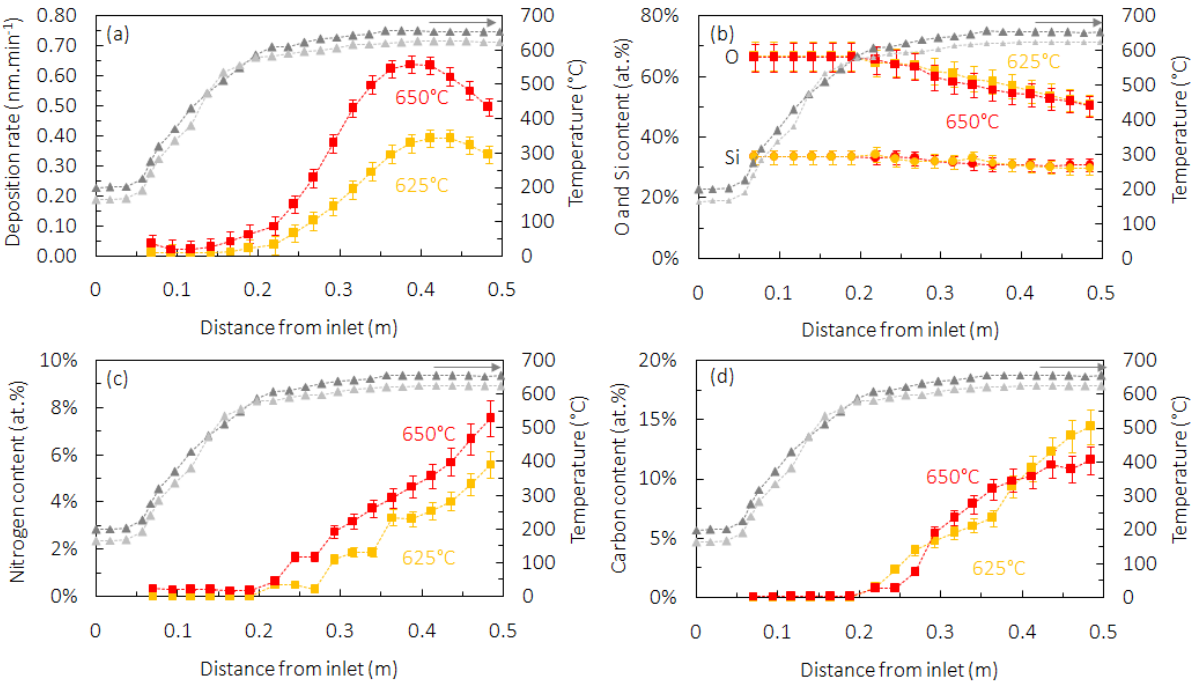


Fig. 3. Influence of the SPT on the average DR (a), oxygen (squares) and silicon (circles) (b), nitrogen (c) and carbon (d) content of the films, for runs performed at 0.6 sccm O_2 at two different SPTs, 625°C (orange data) and 650°C (red data). The temperature profiles for SPT 625°C (light grey) and 650°C (dark grey) are also reported in each diagram.

Fig. 3 (b) shows the O and Si contents of the films, as evaluated by SE. Incorporation of both elements appears to be comparable between the two SPTs. Oxygen shows a decreasing trend as a result of its continuous consumption towards the production of non-film-forming species [15]. Silicon on the other hand remains relatively constant, averaging 32 at.%. The nitrogen content is reported in Fig. 3 (c) and follows a similar trend and shape for both SPTs, namely continuous increase starting at ca. 0.20 m (585°C), reaching a maximum at the end of the probed isothermal zone. However, higher incorporation of N is noted all along the reactor for SPT 650°C, reaching a maximum of 7.5 at.% in contrast to the maximum 5.6 at.% N probed for SPT 625°C. We conclude that nitrogen enrichment is favored at higher temperatures, validating the discussion of Fig. 2 (c). The carbon content, presented in Fig. 3 (d), follows an evolution similar to nitrogen, though its trend is more irregular, lacking any clear distinction between the two SPTs. Carbon incorporation appears to be influenced by multiple factors, such as local temperature, O_2 consumption in the gas phase, as well as intermediate species distribution and concentration.

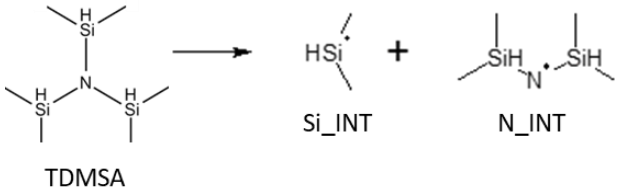
4. Kinetic model development

4.1. Conceptualization of gas phase reactions

Gas phase analysis by GC-MS, NMR, and ESR of the effluent gases at the exit of the reactor for all experimental runs revealed the presence of a common silicon-centered radical species that is produced independently of the applied O_2 flow rate or SPT, as detailed in [15]. This compound was identified to be $Me_2HSi°$, noted Si_INT hereinafter. It originates from the homolytic dissociation of TDMSA at a Si-N bond, a dissociation that produces Si_INT and a nitrogen centered radical, $(Me_2HSi)_2N°$ (a disilazane derivative, noted N_INT hereinafter). Water and at least 15 silicon-containing compounds were also detected [15]. These by-products, presented in Fig. S4 of *Supplementary Material*, were classified into four main categories: silanols, siloxanes, silanamines and an alkoxysilane. The consideration of such a sheer number of compounds - and their associated formation and consumption reactions - in a kinetic model is tedious. For this reason, the obtained information was summarized and utilized to develop an apparent chemical and kinetic model that describes the deposition process with satisfactory accuracy, despite its simplified nature. In that which follows, the considered apparent reactions are presented and justified by concrete quantitative and qualitative experimental results. The

numerous intermediate steps undertaken during the development stages [34] are not detailed explicitly, but are presented in a summarized manner instead.

Inspection of all identified gaseous species (Fig. S4) indicates that Si_INT and N_INT are the building blocks for all compounds detected in the gas phase. Consequently, the dissociation of TDMSA at a Si-N bond appears to be one of the primary gas phase reactions. Quantitative GC-MS analysis of the effluent gases showed that the TDMSA conversion percentage remains at ca. 83 % at SPT 650°C and is insensitive to the presence or absence of O_2 or any variations of its flow rate for the studied range. A preliminary experiment performed at significantly low concentration of oxygen (0 sccm O_2 supplied at the inlet, non-excluding potential microleaks or H_2O desorption from the internal walls of the reactor) also resulted in the production and trapping of the same silicon-centered radical species, with comparable TDMSA conversion percent (81 %). Based on the above results, the TDMSA dissociation reaction was formulated as the first homogeneous reaction of the model, V1 (the notation *V* stands for "volumetric"), leading to the production of the two radicals as follows:



(V1)

The quantitative GC-MS results of TDMSA detected in the reactor effluents for various SPTs (580, 625 and 650°C) in absence of O_2, allowed for the calculation of the kinetic constants of V1, as shown in Fig. 4. A pre-exponential factor of $A_{o,V1}$= $1.68 \cdot 10^{14}$ s^{-1} and an activation energy of $E_{a,V1}$= $2.49 \cdot 10^{2}$ $kJ.mol^{-1}$ were deduced.

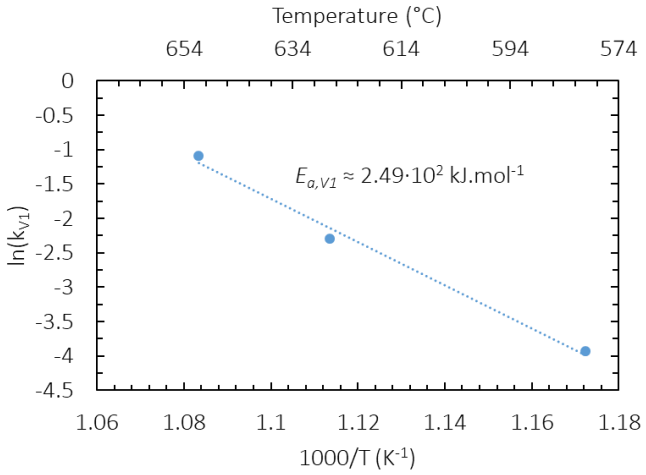
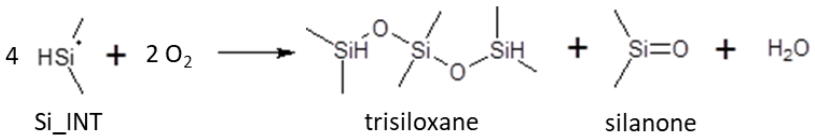


Fig. 4. Arrhenius plot for V1, calculated from quantitative GC-MS analysis of TDMSA at the exhaust of the CVD reactor, supplied under various SPTs.

In order to keep the model complexity low, the produced radical intermediates Si_INT and N_INT are considered as the main reactants that participate in subsequent reactions (be they homogeneous or heterogeneous). Out of the identified gaseous compounds, a number of them include one or two oxygen atoms (Fig. S4). Since O_2 is supplied in the reactor as an oxidant, but is not encountered in V1, it stands to reason that it participates in other reactions. In regards to surface reactions, the involvement of oxygen is evident by its incorporation in the films in Fig. 2 (b) and Fig. 3 (b), and will be discussed in section 4.2. In regards to homogeneous phenomena, volumetric reactions in which O_2 is very likely to participate are those leading to the production of siloxane and/or silanol species. Preliminary trials showed that the formation of these species cannot be ignored if the simulated DR profiles are to conform to the experimental ones [34]. Due to the chemical structure of the identified siloxane and silanol species (Fig. S4) and the absence of a nitrogen atom in them, the Si_INT intermediate was considered as the silicon-atom provider. As such, the apparent reaction V2 was defined, described by the consumption of Si_INT and O_2 towards the production of a siloxane, a silanone and water:



(V2)

The trisiloxane compound produced through reaction V2 is one of the multiple siloxane molecules identified by GC-MS (Fig. S4) and was chosen as a representative compound. Since V2 is an apparent reaction, it encompasses multiple intermediate reactions that eventually lead to the production of the selected trisiloxane compound via the initial production of a silanol (Me_2SiHOH) and a disiloxane ($(Me_2SiH)_2O$), as described in more detail in [15].

Preliminary simulation trials revealed that the presence of O_2 in high concentrations leads to a high consumption of the Si_INT species through reaction V2, decreasing the available Si_INT concentration for subsequent reactions, especially for production of the solid film [34]. Fig. 5 presents a summary of reactions selected from a recent work [15], which are considered to remedy the low Si_INT concentration through its production in other volumetric reactions. We propose that a disiloxane species ($(Me_2SiH)_2O$, as identified by the GC-MS results) can dissociate in the gas phase at a Si-O bond, leading to the production of additional Si_INT ($Me_2SiH°$) quantity and hydrogen radicals (H°) (Fig. 5 (a)). Similarly, a disilazane compound ($(Me_2SiH)_2NH$, as identified by GC-MS) can also dissociate at a Si-N bond, leading to Si_INT and H° production (Fig. 5 (b)). As a result, the Si_INT deficiency can be balanced out. These two dissociation reactions also lead to the production of silanone ($Me_2Si=O$) and silanimine ($Me_2Si=NH$) compounds, respectively.

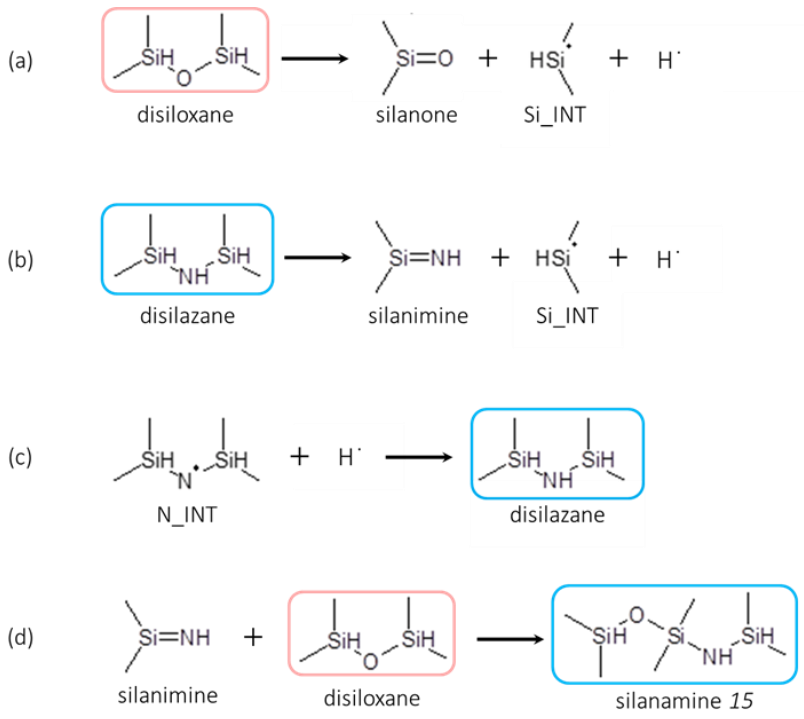
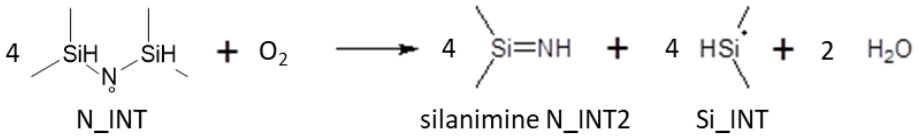


Fig. 5. Supplementary gas phase reactions leading to the production of a silanone and Si_INT (a), a silanimine noted N_INT2 and Si_INT (b), a disilazane (c) and the silanamine compound *15* (d), considered for the development of the apparent SiO_xN_y model.

The production of silanone is already accounted for in reaction V2. Thus, the apparent volumetric reaction V3 that is formulated in order to produce additional Si_INT, was conceptualized based on the dissociation reaction of the disilazane molecule $(Me_2SiH)_2NH$ (Fig. 5 (b)). It is noted that the formation of the disilazane molecule proceeds through a reaction of the N_INT intermediate species ($(Me_2HSi)_2N°$) with a H radical (Fig. 5 (c)). The H radical can be produced through a preceding reaction, such as the dissociation of the disiloxane molecule (Fig. 5 (a)). To avoid the implementation of multiple cascading reactions and in order to keep the model complexity as low as possible, the apparent reaction V3 was formulated as the direct reaction of the N_INT radical intermediate with O_2, after several trials and comparisons between experimental and calculated results. V3 leads thus to the production of Si_INT, water and a second nitrogen-containing intermediate, noted N_INT2:



(V3)

The produced N_INT2 is defined as an intermediate compound from a family of nitrogen-containing molecules related, but not exclusive to, silanimines, produced through the homolytic dissociation of the disilazane compound [15], as shown in Fig. 5 (b). It is noted that N_INT2 is a fictitious species and was not detected in the gas phase by GC-MS. However, the high reactivity and fast consumption of such silanimine compounds would explain the difficulty in probing them.

Reaction V3 serves multiple causes. One is the already discussed supplementary production of Si_INT for higher O_2 flow rates, in order to balance out the high Si_INT consumption through reaction V2. To achieve this, it was necessary to add O_2 as a reactant in V3. The second reason for V3 was the requirement for the production of a species that can introduce carbon in the films. Fig. 6 (a) presents the total and individual thickness profiles of the three components (SiO_2, Si_3N_4 and amorphous-C) considered in SE for 0.6 sccm O_2 at SPT 650°C. The thickness profiles of the other runs are comparable. The results reveal that the deposition of an oxide-rich material is proceeding first, while the incorporation of a nitride-type material and carbon is initiated later in the reactor, both at approximately the same region to

each other. The deposition of an oxide-rich material closer to the inlet is illustrated more clearly by plotting the evolution of x and y of the $SiO_xN_yC_z$ stoichiometry as a function of the position in the reactor, as shown in Fig. S5 of *Supplementary Material*. To keep the model complexity as low as possible, it is assumed that carbon is inserted in the films through the same species that also introduces nitrogen. The continuous evolution of the carbon and nitrogen contents in the films, as shown previously in Fig. 2 (c) and (d), is also recalled. The atomic C/N ratio along the length of the reactor calculated from these values is presented in Fig. 6 (b). In the 0.35-0.5 m region, considered due to the more pronounced incorporation of C and N in it, the average C/N ratio is 2.1, 1.9, and 2.9 for 0.3, 0.6 and 1.2 sccm O_2, respectively. It is underlined that the maximum C/N ratio is in fact noted for the highest O_2 flow rate.

Combining the above, a species that inserts C and N in the films is needed, and its production should ideally depend on O_2 concentration to replicate the higher C/N ratio at the higher O_2 flow rate. Although TDMSA and N_INT fit the first requirement, only N_INT2 fits the full profile. Thus, the N_INT2 intermediate produced through V3 is considered responsible for the insertion of carbon in the films through its participation in surface reactions that will be discussed in section 4.2. Due to the assumption that carbon is incorporated together with nitrogen, the sum of the Si_3N_4 and amorphous-C components considered in SE are collectively referred to as “total Si_3N_4" hereinafter.

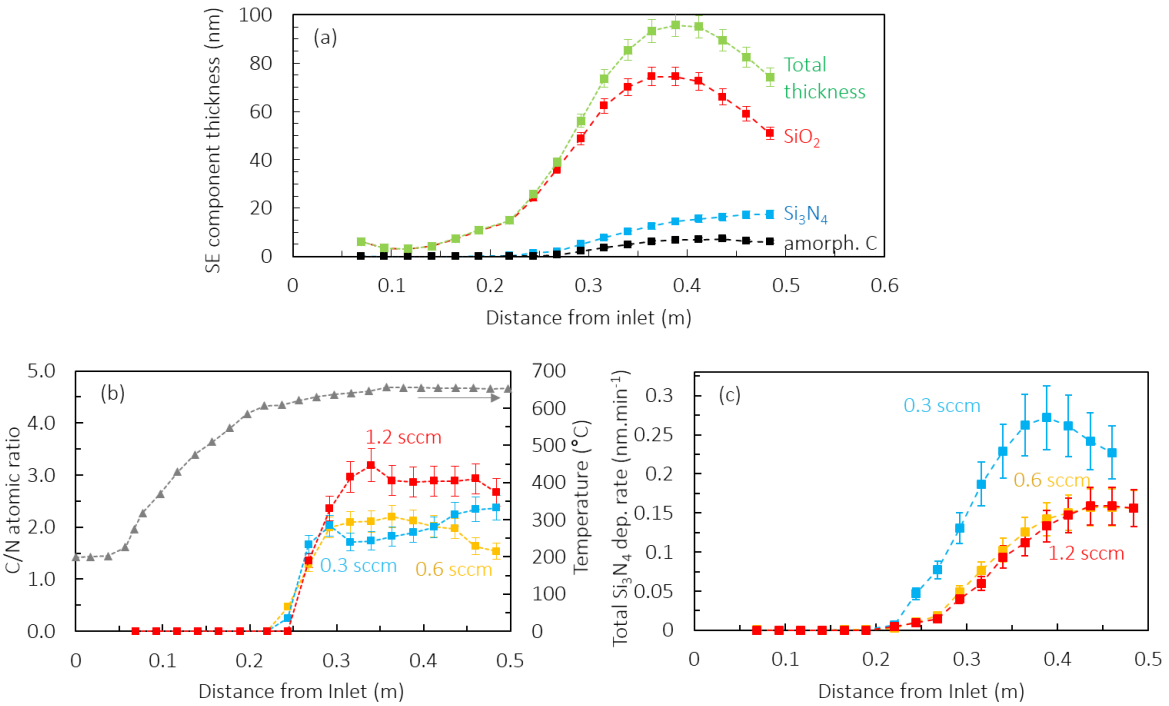
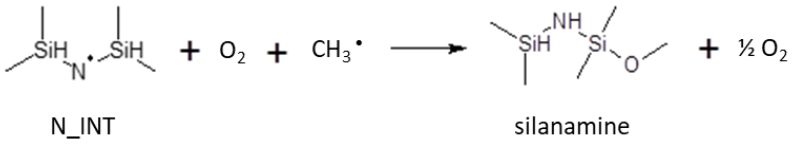


Fig. 6. Experimental results measured by SE. Total thickness for run performed at 0.6 sccm O_2 and SPT 650°C and individual thickness of the three SE components (SiO_2, Si_3N_4 and amorphous C) (a). Evolution of atomic C/N ratio for varying O_2 flow rates at SPT 650°C (b). DR of the total Si_3N_4 phase for varying O_2 flow rates at SPT 650°C (c).

At the same time, the above formulation would naturally translate in a globally higher N_INT2 concentration available in the gas phase for higher O_2 partial pressure, and by extension increased reaction rates of any solid phase reactions in which N_INT2 participates as a reactant. In this case, higher deposition rates of nitride material would be observed whenever high O_2 concentrations are supplied in the reactor, something that would contradict the experimental results. Inspecting the total Si_3N_4 deposition as deduced from SE (Fig. 6 (c)), it is apparent that the produced films are less nitrogen rich under more oxidizing atmospheres. To account for this behavior, a fourth volumetric reaction, V4, was conceptualized, aiming to decrease the available concentration of N-containing species in the gas phase under higher O_2 flow rates. Such a reaction is highly likely, given the detection of silanamine compounds with a Si-N-Si-O sequence [15]. The apparent reaction V4 was therefore defined as follows:



N_INT silanamine (V4)

Constituting the initial building block of the silanamine compound, the N_INT intermediate was directly used as the reactant, in order to by-pass the requirement for multiple cascading reactions [15] and reduce model complexity. The methyl radical reactant can originate from dissociation reactions at any Si-C bond of the TDMSA precursor and/or any Me_2Si-containing compounds [15]. For simplicity, such dissociation reactions are not described explicitly in the model, therefore the involvement of the methyl radical in V4 is supposed, but not implemented in the actual simulations. Globally, reaction V4 serves to reduce the available concentration of N_INT under higher O_2 flow rates, modulating thus the production of N_INT2 as well and indirectly serving to replicate the competitive incorporation of O and N. This is essential for reproducing the lower nitrogen incorporation encountered in runs performed under more oxidizing atmospheres (Fig. 6 (c)).

Although V4 reduces N_INT concentration by consuming it, N_INT2 production through V3 is still substantially increased under higher O_2 flow rates, given that O_2 participates as a co-reactant. Attempts to adjust the kinetic constants and partial order exponents of V3 and

V4 did not yield satisfactory results, making it clear that the model had to be enriched with an additional volumetric reaction, in order to fit the simulations as close as possible to the experimental results. Inspection of the compounds identified by GC-MS points at the production of another silanamine species with a Si-N-Si-O-Si sequence (N-(dimethylsilyl)-1-[(dimethylsilyl)oxy]-1,1-dimethylsilanamine, compound ***15*** in Fig. S4 of *Supplementary Material*). In a recent work [15], it was proposed that its production occurs through a volumetric reaction between the silanimine intermediate N_INT2 and a disiloxane molecule (Fig. 5 (d)). This reaction is represented by a simplified, apparent volumetric reaction V5 in the model, formulated with the N_INT2 reactant being transformed into non-film-forming by-products of the silanamine family:

$$N_INT2 \rightarrow by\text{-}products \qquad \text{(V5)}$$

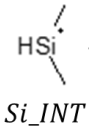
The participation of O_2 or Si_INT in reaction V5 was not considered, in order to not influence other reactions in which these two molecules are involved.

4.2. Conceptualization of surface reactions

As shown in Fig. 2 (d) and Fig. 3 (d), the produced material is a SiO_xN_y film containing a non-negligible amount of carbon. An ambitious attempt during the development process of the deposition mechanism was to not only simulate local DR values, but also the local concentration of N and C into the films. Fig. 2 (b), (c) and (d) illustrate that the composition of the carbonated SiO_xN_y material evolves along the length of the reactor, influenced by the local temperature and gas phase composition. Thus, it would be incorrect to define film formation through one single surface reaction; this would translate into the deposition of a film with constant composition throughout. Therefore, at least two surface reactions are required: one leading to the formation of silicon oxide and one to the formation of silicon nitride, with the insertion of C considered at least in one of them. Obviously, the deposited material is a homogeneous, amorphous carbonated SiO_xN_y as revealed by HRTEM analysis [34], instead of the conglomeration of SiO_2 and Si_3N_4. Despite this, the definition of separate, apparent, surface reactions for each compound allows for the independent tweaking of their respective deposition rates, which in turn provides control of the resulting film composition.

Consequently, the direct contribution of Si_INT, N_INT and N_INT2 to the solid film is considered, leading after trials to three apparent surface reactions, S1, S2, and S3, which account for the production of materials with distinct stoichiometries; SiO_2, Si_3N_4 and carbonated-Si_3N_4 material ($Si_3N_4C_{12}$), respectively, as explained below.

The SE results were extensively used for the definition of the surface reactions and their kinetic constants, based on various assumptions already discussed in section 4.1. It is recalled that the material deposited closer to the inlet is systematically more rich in oxygen, as observed by the high O content in the films (Fig. 2 (b)), the fitting of the SE spectra to a primarily SiO_2-type material from 0-0.25 m (Fig. 6 (a)) and the x value of the $SiO_xN_yC_z$ stoichiometry being close to 2 (Fig. S5). As already mentioned, it is assumed that C and N are inserted through the same species, given the very close locality and similar trends of the individual Si_3N_4 and amorphous-C components (Fig. 6(a)). As a result, it is considered that the apparent surface reaction S1 leads to the deposition of carbon-free SiO_2 as follows:



$$Si_INT + O_2 \rightarrow SiO_2 + by\text{-}products \qquad \text{(S1)}$$

Fig. 7 presents the Arrhenius plot of S1 for the three runs at SPT 650°C, using the logarithm of the kinetic constant k_{S1} of S1, which is calculated from the DR of the SiO_2 component based on the rate law of S1 ($S1 = k_{S1}[Si_INT]^a[O_2]^b$). First order kinetics were considered initially. The concentrations of both reactants for each run are extracted from simulation of reaction V1 using FLUENT®. Only samples between 0.2 m and 0.4 m (square symbols in Fig. 7) were considered for extraction of the kinetic parameters, since significant O_2 consumption is taking place beyond 0.4 m, as reflected in the decreasing k_{S1} values at higher temperatures (triangle symbols). Additionally, inspection of the SiO_2 component thickness in Fig. 6(a) hints at a potential different deposition mechanism in the 0.0-0.2 m range. Thus, samples between 0.0 and 0.2 m were not considered since the primary oxide-rich material in this region would bias the kinetics of the apparent reaction S1. From the slope and intercept of Fig. 7 an initial activation energy $E_{a,S1}$= $3.57 \cdot 10^1$ kJ.mol^{-1} and a pre-exponential factor $A_{o,S1}$= $1.79 \cdot 10^{-3}$ s^{-1} were deduced. It is noteworthy that the slope of each individual run is similar, indicating consistency of the S1 activation energy among these experiments. However, the intercept is different, hinting at an uncertainty of the calculated $A_{o,S1}$ value.

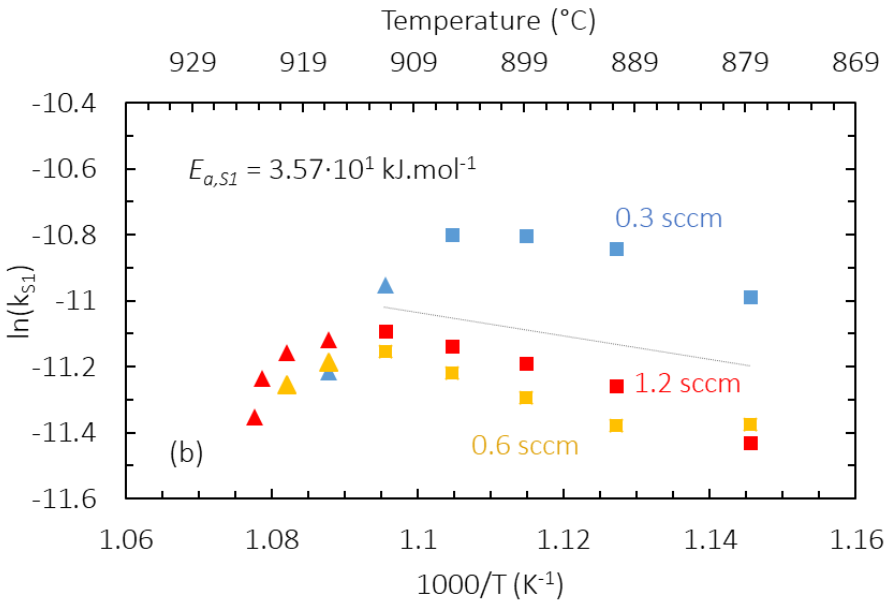


Fig. 7. Arrhenius plot of k_{S1}, for SiO_2 production through S1, calculated for selected samples (squares) from runs using varying O_2 flow rates at SPT 650°C.

In regards to C and N, in order to formulate representative, apparent reactions for the deposition of a carbonated Si_3N_4 material, the C/N atomic ratio calculated by SE is considered initially (Fig. 6 (b)). At 1.2 sccm O_2, the C/N ratio between 0.35-0.5 m appears constant at around 2.9, indicating that a nitrogen-containing intermediate with three $–CH_3$ ligands is potentially participating in film formation. Between 0 and 0.35 m, the C/N atomic ratio is lower than 2.9 and presents an increasing trend. This could be likely related to the higher local O_2 concentrations in that region, resulting in more efficient oxidation and cleaving of the organic ligands of the gaseous compounds. Similar trends are observed for the other two runs.

Such general evolution of the C/N ratio could indicate two possibilities: in a first scenario, the CH_3-cleaving step is taking place in the gas phase prior to deposition, meaning that the primary nitrogen-containing intermediate, N_INT, “loses” part of its four methyl moieties before participating in film-forming reactions. In a second scenario, two (or more) nitrogen-containing intermediates, each containing a different number of carbon atoms, participate in film formation and result in varying incorporations of carbon, depending on their kinetics. The problem with the first scenario is that it relies on O_2 to cleave the carbon of the N_INT. However, the higher C/N ratio at the highest O_2 flow rate (1.2 sccm) does not support this mechanism. Therefore, the second scenario is considered and two apparent surface reactions, S2 and S3, are assumed. Since the experimentally determined C/N atomic ratio spans

from 0 to ca. 3, we assume the two extreme stoichiometries: Si_3N_4, i.e. $Si_3N_4C_0$ for S2, and $Si_3N_4C_{12}$ for S3:

$$4\ N_INT \rightarrow\ Si_3N_4 + by\text{-}products \quad \text{(S2)}$$

$$4\ N_INT2\ \rightarrow Si_3N_4C_{12} + by\text{-}products \quad \text{(S3)}$$

S2 results in the deposition of a nitride material with no carbon, assuming complete cleaving of the $–CH_3$ moieties in the N_INT intermediate after adsorption on a solid surface, while S3 leads to the deposition of a carbonated $Si_3N_4C_{12}$ material, without cleaving of any organic ligands. Since higher C/N ratio is found at higher O_2 flow rate, N_INT2, the production of which is dependent on O_2 concentration through reaction V3, is considered as the reactant of S3. Reaction S3 is then assumed as the primary reaction taking place for 1.2 sccm O_2. An initial activation energy of $E_{a,S3}$= $1.97 \cdot 10^2$ kJ.mol^{-1} is deduced from the SE data of the total Si_3N_4 deposition at 1.2 sccm O_2, after their formulation in an Arrhenius plot considering first order kinetics. Following that, the difference in nitride deposition noted between 1.2 and 0.3 sccm O_2 is used to extract an initial activation energy of $E_{a,S2}$= $3.51 \cdot 10^1$ kJ.mol^{-1} for S2.

It is noted that initial formulations of S2 and S3 included N_INT and O_2 as the reactants in both reactions, assuming the removal of different amounts of superfluous $–CH_3$ moieties through the oxidation of N_INT on solid surfaces. However, participation of O_2 in the production of Si_3N_4 or $Si_3N_4C_{12}$ results in higher total Si_3N_4 deposition rates for higher O_2 flow rates, which is contrary to the experimental results (Fig. 6 (c)). Therefore, the simulation results demonstrated that O_2 should not participate in any of these two apparent surface reactions and that the cleaving of $–CH_3$ groups in the N_INT species should instead preferably happen through a volumetric reaction involving N_INT and O_2. This reaction is represented by the already discussed apparent reaction V3. For S2, the cleaving of the $–CH_3$ moieties in N_INT is assumed to occur directly on the solid surfaces.

It is important to note that hydrogen is not considered in the composition given by SE. Complementary SE components such as H_2O or any components that could represent the N-H incorporation observed in the FT-IR spectra (Fig. S2) were not included. The distribution of hydrogen itself across various species (H_2O, Si-OH, $-CH_3$, N-H, CH_x), did not allow its assignment to the amorphous-C component. For this reason the involvement of hydrogen was not accounted for in any of the defined stoichiometries for the apparent heterogeneous reactions S1, S2 or S3.

4.3. Proposed SiO_xN_y kinetic model

In summary, reaction V1 represents the decomposition of the TDMSA precursor, in order to produce the two main building blocks: Si_INT and N_INT. These two intermediates are then encountered in all gaseous by-products identified by GC-MS. Reaction V2 serves towards the consumption of O_2 and Si_INT to produce the family of siloxane by-products. More than just representing the production of an identified family of by-products, reaction V2 also serves to reduce the Si_INT concentration available for SiO_2 deposition through reaction S1. Through this, the bell shape of the SiO_2 component thickness (Fig. 6 (a)), originating from a depletion-phenomenon, can be replicated. Reaction V3 compensates for the Si_INT deficit (brought forth by reactions V2 and S1) by producing Si_INT under high O_2 concentrations, and simultaneously serves the production of a carbonated nitrogen-containing intermediate, N_INT2, the concentration of which depends on that of O_2. V3 thus also addresses the higher C/N ratio observed for the highest O_2 flow rate. V4 represents the consumption of N_INT through reaction with O_2 to produce the silanamine family of by-products, with the main aim to decrease the global available N_INT quantity in the gas phase at higher O_2 flow rates and replicate the competitive incorporation of O and N, which results in the reduced total Si_3N_4 DRs for 0.6 and 1.2 sccm (Fig. 6 (c)).

Consideration of all solid phase and gas phase results led to the formulation of an apparent kinetic model comprising 11 species and 8 reactions in total. Through its stepwise enrichment, the kinetic constants of reactions V2 to V5 and S1 to S3 were calculated and refined in an iterative manner, by systematic comparison between experimental and simulation results. The kinetic constants of V1 were kept as calculated, since they originated from quantitative GC-MS results. Table 1 summarizes the final version of the considered apparent chemical reactions and their respective kinetic laws and constants.

Table 1: Proposed apparent chemical model for carbonated SiO_xN_y deposition from TDMSA and O_2, with list of reactions and their respective kinetic laws and constants.

	Reaction	Rate law	Kinetic constants
	Volumetric Reactions (kmol.m^{-3}.s^{-1})		
V1	$TDMSA \rightarrow Si_INT + N_INT$	$k_1[TDMSA]$	$k_1 = 1.68 \times 10^{14} \times exp\left(-\frac{29954.1}{T(K)}\right)$
V2	$4\ Si_INT + 2\ O_2 \rightarrow siloxane + bp$	$k_2[Si_INT]^a[O_2]^b$ $a = 0.50, b = 1.00$	$k_2 = 1.98 \times 10^{14} \times exp\left(-\frac{25201.1}{T(K)}\right)$
V3	$N_INT + O_2 \rightarrow N_INT2 + Si_INT + bp$	$k_3[N_INT]^a[O_2]^b$ $a = 0.80, b = 0.85$	$k_3 = 2.96 \times 10^{18} \times exp\left(-\frac{29808.7}{T(K)}\right)$
V4	$N_INT + O_2 \rightarrow silanamine + bp$	$k_4[N_INT]^a[O_2]^b$ $a = 0.45, b = 1.26$	$k_4 = 2.96 \times 10^{20} \times exp\left(-\frac{32334.4}{T(K)}\right)$
V5	$N_INT2 \rightarrow bp$	$k_5[N_INT2]$	$k_5 = 6.276 \times 10^{28} \times exp\left(-\frac{59575.2}{T(K)}\right)$
	Surface Reactions (kmol.m^{-2}.s^{-1})		
S1	$Si_INT + O_2 \rightarrow SiO_2 + bp$	$k_{s1}[Si_INT]_s^a[O_2]_s^b a$ $= 0.40, b = 0.37$	$k_{s1} = 7.25 \times 10^{-2} \times$ $exp\ exp\left(-\frac{7598.5}{T_s(K)}\right)$
S2	$4\ N_INT \rightarrow Si_3N_4 + bp$	$k_{s2}[N_INT]_s^a$ $a = 0.70$	$k_{s2} = 6.27 \times 10^6 \times exp\left(-\frac{29080.4}{T_s(K)}\right)$
S3	$4\ N_INT2 \rightarrow Si_3N_4C_{12} + bp$	$k_{s3}[N_INT2]_s^a$ $a = 0.50$	$k_{s3} = 8.61 \times 10^6 \times exp\left(-\frac{29065.5}{T_s(K)}\right)$

Note: *Ts* is the temperature of the solid surface. The notation *bp* stands for "by-products".

5. Simulation results and discussion

As a first visual validation, Fig. 8 presents a comparison between the experimental thickness (Fig. 8(a)) and simulated deposition rate profiles (Fig. 8(b)) for all three runs, resulting from the implementation of the developed kinetic model into FLUENT®. The iridescences observed in the photographs of the array of Si substrates after deposition (Fig. 8 (a)) are caused by interference of the deposited SiO_xN_y material with the light and signify changes in thickness. Since the material of interest is a type of SiO_xN_y, the produced color palette is expected to deviate from that of pure SiO_2 and Si_3N_4. It is noted that the iridescences from Si_3N_4 films appear more vibrant than those of SiO_2 [35], thus the brighter colors noted for 0.3 sccm O_2 could indicate higher N incorporation, which is indeed the case as observed in Fig. 2 (c). For all three runs, deposition is initiated beyond samples pH or pI, and a characteristic flow pattern is observed due to the high total gas flow rate and the progressive film formation as a result of the thermal gradient. Decreased film deposition is observed on the final samples of the array. This reduction in film formation is initiated on sample p2 for 0.3 sccm O_2, but noted only after sample p6 for 1.2 sccm O_2. This behavior is connected to the eventual depletion of the available O_2 concentration due to its consumption in homogeneous and heterogeneous reactions. Fig. 8 (c) shows the O_2 concentration, extracted from a horizontal line passing through the middle of the samples array. It reveals well the depletion of O_2 earlier in the reactor, i.e. closer to the inlet for 0.3 sccm O_2, when compared to 1.2 sccm O_2.

Fig. 8 (b) presents the total DR contours, namely the sum of all surface reactions (S1, S2, and S3), as calculated from the model. It is pointed out that Fig. 8(a) portrays distribution of thickness, while Fig. 8(b) shows distribution of deposition rates. Despite this difference, by assuming steady state and a minimal incubation time, the two values can be compared to each other, since a locally higher deposition rate will logically lead to a locally higher film thickness. Globally, it is observed that the simulations reproduce the general shape of the experimental profiles, validating the model in shape. The peripheral area of reduction in the total deposition rate as a result of the O_2-depletion is also encountered (white arrows), with the simulations correctly representing its occurrence earlier for 0.3 sccm O_2 and its displacement towards the right-most samples (p5/p6) for 1.2 sccm O_2.

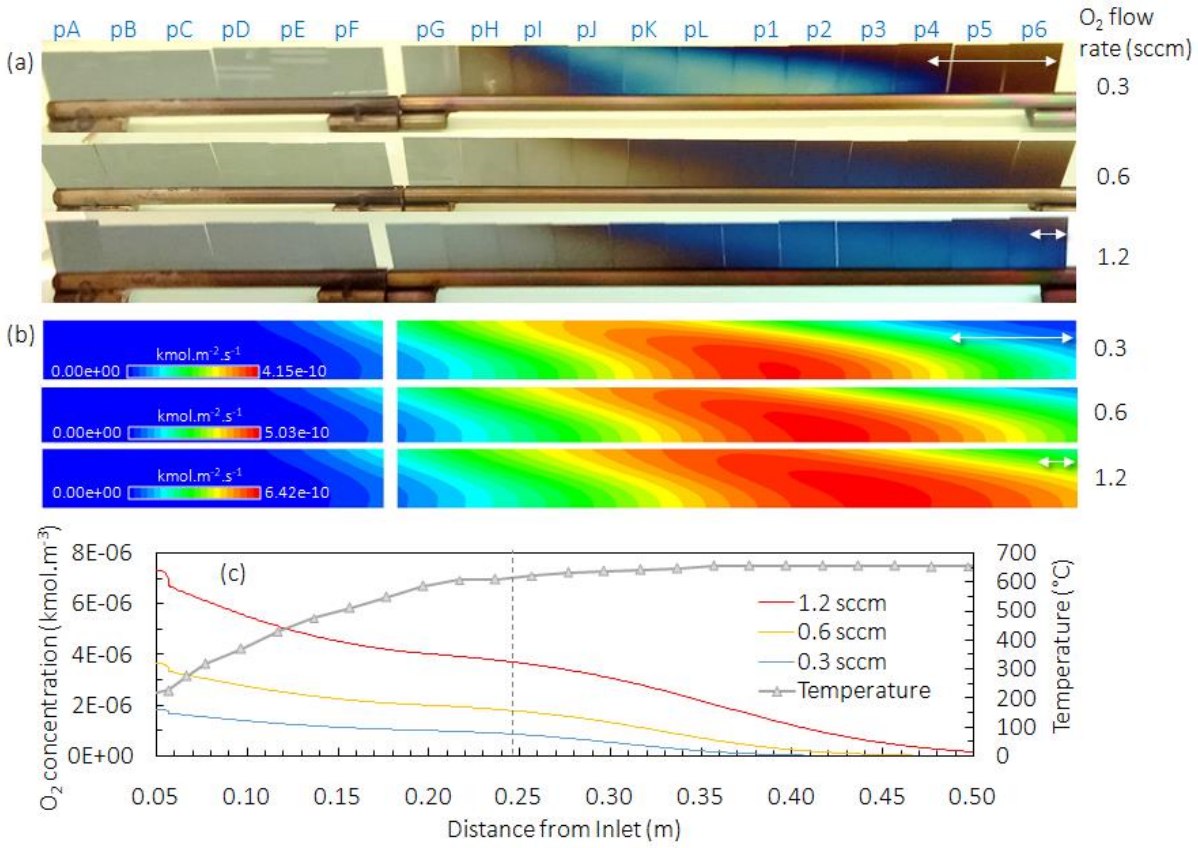


Fig. 8. Photographs of array of samples after deposition (a), simulated total DR profiles (b) and O_2 concentration extracted from model (c), for various O_2 flow rates at SPT 650°C. Vertical dashed line in (c) signifies the position of sample pH.

Fig. 9 shows local values of DR and composition measured by SE and compares them to those calculated by the model for all runs at SPT 650°C. Unlike the values used for the development of the model –which were the average of 5 points– the data presented in Fig. 9 are local values probed at the center of each sample. For the model, a horizontal line passing across the middle of all samples is utilized to extract the corresponding values from FLUENT®.

As illustrated in Fig. 9 (a) to (c), the DR profiles of the SiO_2 (through S1) and total Si_3N_4 depositions (through S2 and S3) are well represented for all three runs. The closest agreement is observed for the run performed at 1.2 sccm O_2 (Fig. 9 (c)). It is also noted that the bell-shape of the SiO_2 DR profile is reproduced for all three runs, with slight deviations. More specifically, an overestimation of the SiO_2 DR is noted beyond 0.3 m for 0.3 sccm O_2 (Fig. 9 (a)). For the run at 0.6 sccm O_2 (Fig. 9 (b)), the SiO_2 DR is slightly overestimated from 0 to 0.4 m, after which it is underestimated. A slight overestimation of the SiO_2 DR is also noted across the whole reactor for the run at 1.2 sccm O_2 (Fig 9 (c)).

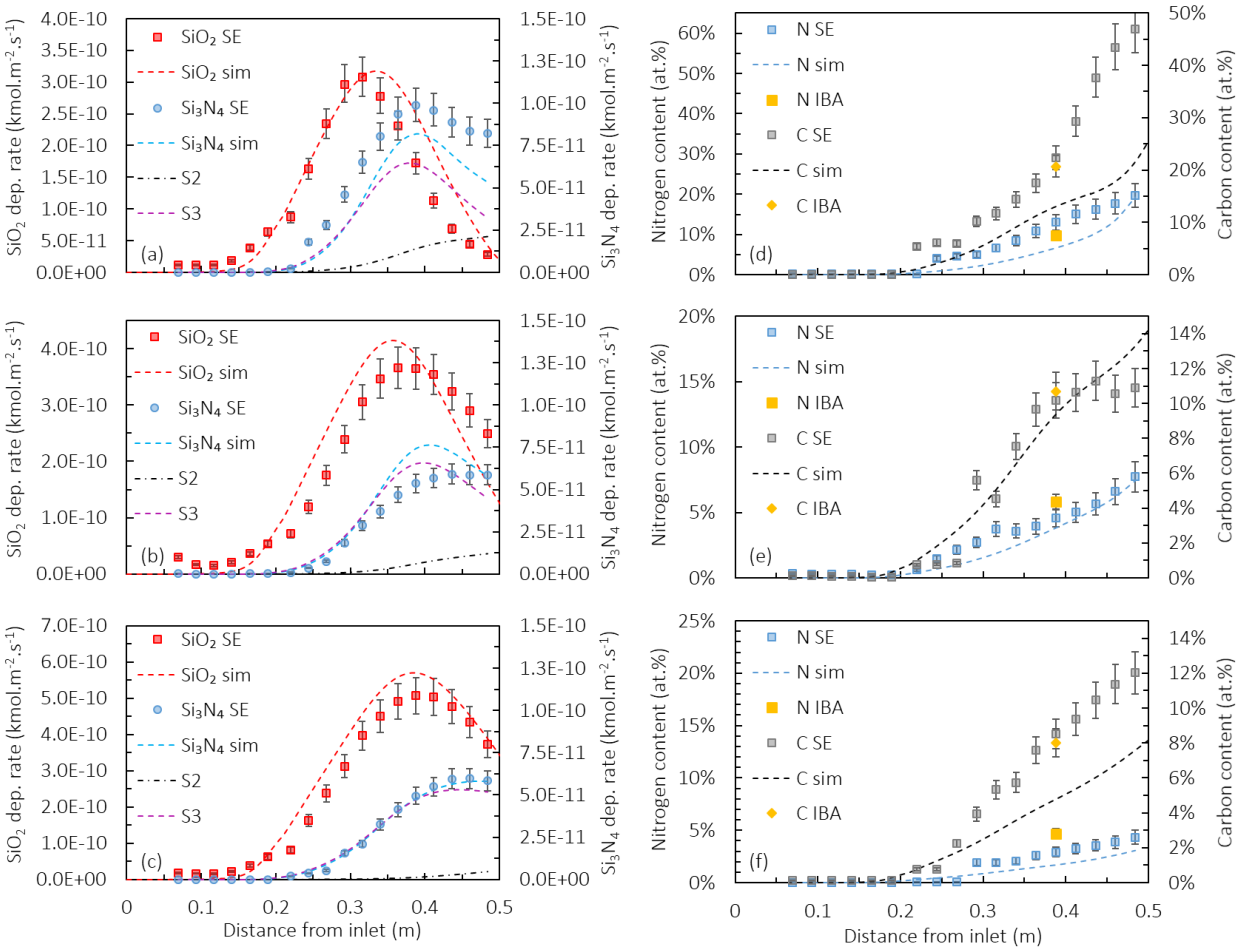


Fig. 9. Comparison of local simulated (dashed lines) and experimental (filled symbols) SiO_2 and total Si_3N_4 DR for 0.3 (a), 0.6 (b) and 1.2 sccm O_2 (c), alongside contribution of S2 and S3 to the total Si_3N_4 DR. Comparison of local composition in C and N between simulations and experimental values for 0.3 (d), 0.6 (e) and 1.2 (f) sccm O_2. Yellow points show C and N composition measured by ion beam analyses on the p2 sample of each run.

In regards to total Si_3N_4 deposition, Fig. 9 (a) to (c) illustrate its distribution between S2 and S3. For all three runs, S3 is observed to contribute more than S2. For 1.2 sccm O_2 (Fig. 9 (c)), S2 has decreased significantly and S3 is the primary nitrogen-depositing reaction. This is a direct result of the N_INT consumption through V4 and the higher N_INT2 production through V3 as the O_2 supply increases.

Some discrepancies are noted in the total Si_3N_4 DR profile. At 0.3 sccm O_2 (Fig. 9 (a)), the total nitride deposition is underestimated, most likely due to the rate-limiting nature of O_2.

The low O_2 concentration for this run results in low production of N_INT2 through reaction V3 and therefore lower nitride production through S3. Once O_2 supply is increased to 0.6 sccm, the total Si_3N_4 DR is observed to increase, with the simulations overestimating the experimental data in the 0.3-0.5 m region (Fig. 9 (b)). This behavior is linked to the higher production of N_INT2 through V3, thanks to the additional oxygen concentration. At 1.2 sccm O_2 on the other hand (Fig. 9 (c)), the total Si_3N_4 DR profiles present an excellent agreement between the calculated and experimental local data. In this run, the supplied oxygen is higher, meaning the reaction rate of V4 is also increased. Through this, an adequate N_INT quantity is consumed towards the production of non-film forming intermediates, leaving therefore less N_INT available for the production of N_INT2. As a result, reactions V3, V4 and V5 balance each other out.

The comparison of the local compositions in N and C for all three runs is shown in Fig. 9 (d) to (f), respectively. More accurate N and C composition results that were obtained by IBA on selected samples are included in yellow for reference. The gradually increasing trends are well represented for all runs, with deviations still persisting however. For the run at 0.3 sccm O_2 (Fig. 9 (d)), a general underestimation is noted for both elements. This underestimation is attributed to the overestimation of the SiO_2 DR on one hand, and the underestimation of the total Si_3N_4 DR on the other (Fig. 9 (a)). This results namely in Si and O occupying larger composition percentages of the film in relation to N and C. A closer agreement is observed for the simulated composition of both elements for 0.6 sccm O_2 (Fig. 9 (e)). For 1.2 sccm O_2 on the other hand, the simulated composition in both C and N is underestimated once more (Fig. 9 (f)) as a result of the SiO_2 DR overestimation in Fig. 9 (c). A summary of the deviations observed for each set of values for all runs is included in section 6 of *Supplementary Material*. It is pointed out that the largest deviations are noted for the simulated carbon content in particular. A potential reason could be the various assumptions that were adopted for the development of the apparent chemical model. More specifically, only one deposition reaction, S3, is considered to describe the incorporation of carbon in the films, with an assumed stoichiometry of $Si_3N_4C_{12}$. In reality however, all produced gaseous species that were detected by gas phase analyses (Fig. S4) contain a certain amount of carbon, meaning that it is very likely for S1 and S2 to also be responsible for insertion of carbon in the films, with SiO_xC_y and $Si_xN_yC_z$ stoichiometries, respectively.

Fig. 10 presents a set of contours extracted for the run performed at SPT 650°C and 1.2 sccm O_2, after implementation of the developed kinetic model. Contours of gas velocity, gas

temperature and all species mass fractions are plotted along a XZ plane that crosses the center of the reactor. The contours for all volumetric and surface reactions are plotted along the YZ plane that crosses the array of samples.

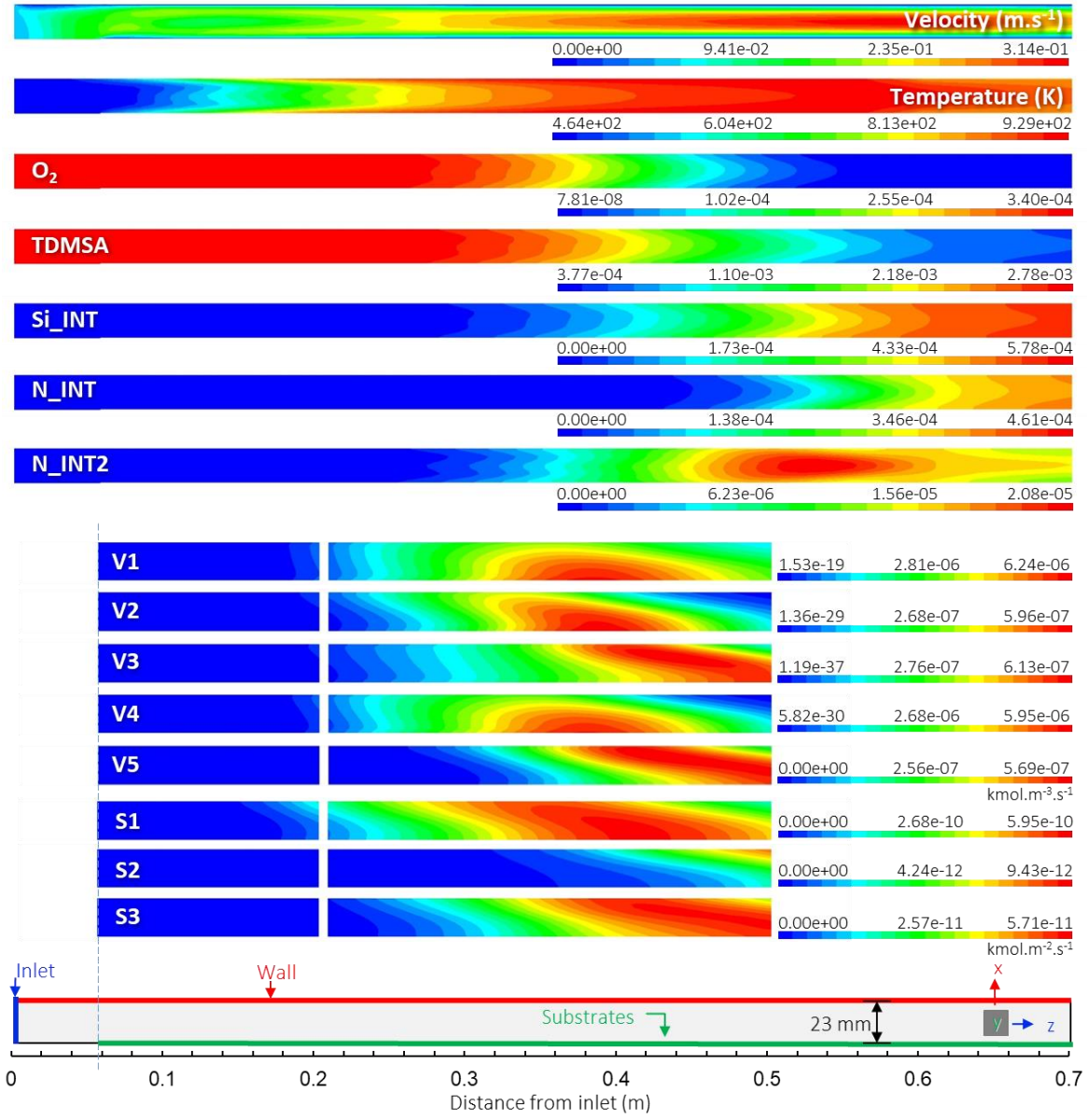


Fig. 10. Gas velocity, temperature and species mass fraction profiles in the gas volume (XZ plane) and reaction rates near the samples surface (YZ plane) for the run performed at SPT 650°C and 1.2 sccm O_2.

The velocity profile presents a parabolic shape, as classically observed for laminar gas flow. A maximum velocity of 0.31 $m.s^{-1}$ is observed in the hottest zones of the reactor. The

temperature of the gas remains below 200°C in the inlet region, increasing as it traverses through the heated reactor, with its bulk being naturally colder than the portion closer to the reactor walls and the substrates. Between 0.1 and 0.3 m, the temperature profile presents a W shape. This emerges as the result of a double vortex trajectory of the gas in the inlet region, which has been explained in more detail elsewhere [27]. This W shape is also observed in the mass fraction profiles.

The mass fractions of the principal species of the developed model are also presented in Fig. 10. Most mass fractions present a W shape from 0 to ca. 0.4 m. Beyond 0.4 m, a parabolic shape occurs, in good accordance with a fully developed laminar flow. A first observation is that the quantity of O_2 exiting the reactor appears to have drastically decreased, which is the result of its participation and consumption in multiple reactions. The mass fraction of TDMSA is also decreasing with the traversal of the gas through the reaction chamber. A portion of it is still exiting the reactor however, corresponding to a conversion rate of 85.9 %. This value favorably compares to 82 % measured experimentally by quantitative GC-MS at the exit of the reactor for this specific run. The consumption of TDMSA occurs through reaction V1, which dictates Si_INT and N_INT production. As expected, the mass fractions of these two species start at zero and increase further in the reactor, upon the heating of the gas volume and the onset of V1. Si_INT is encountered at ca. 0.35 m and onwards. Since both Si_INT and N_INT are produced through the same reaction V1, one would expect N_INT to appear in that locality as well. Contrary to that however, notable quantity of N_INT is observed only beyond ca. 0.5 m, the reason being reactions V3 and V4, which consume O_2 and N_INT to produce N_INT2 and a silanamine, respectively. Thus, as soon as N_INT is produced through V1, a significant portion of it is consumed. This claim is backed up by the onset of the N_INT2 mass fraction after 0.35 m, a region where N_INT was originally expected to be found. The mass fraction profile of N_INT2 itself presents a profile distinct from the other species. Its distribution is the result of an initially high N_INT2 production through V3 due to the presence of sufficient O_2, alongside concomitant consumption through V5 and S3, which become more pronounced in relation to V3 once the O_2 concentration has decreased.

Fig. 10 also shows the distribution profiles of the reaction rates for all formulated reactions. Out of the volumetric reactions, the two most prominent ones are V1 and V4, namely the homolytic dissociation of TDMSA towards Si_INT and N_INT (V1) and the consumption of the N_INT species after reaction with O_2 (V4). Additionally, in regards to reactions that involve N_INT, reaction V4 and V3 are noted to initiate at 0.2 and 0.25 m, while S2 is observed

only after the reaction rate of V4 decreases to almost zero. This indicates the more predominant reaction of N_INT with O_2 (reactions V3 and V4), compared to its delayed participation in film formation through reaction S2. Lastly, out of the surface reactions, reaction S1, namely the deposition of a SiO_2 material, is the most prominent, with a reaction rate of at least one order of magnitude higher than the two nitride-depositing reactions, S2 and S3. Additionally, S1 begins at ca. 0.2 m, further upstream compared to S2 and S3. This is in good correlation with the more oxide-rich character of the films noted at the region closer to the inlet (Fig. 6 (a) and Fig. S5). Between the two nitride-depositing reactions S2 and S3, S3 exhibits reaction rates almost one order of magnitude higher than S2. Globally, this higher reaction rate combined with the broader distribution of S3, explains and replicates well the incorporation of significant quantity of carbon in the produced SiO_xN_y films.

In light of all presented results, it is underlined that the present work subscribes to a long series of modeling of CVD processes, starting in the 80s with the insight in the CVD of Si from silane [36, 37] until recently [38], with the modeling of the deposition of unary metallic [39, 40] and simple ceramic (oxides, carbides) films [23, 27, 41, 42]. Despite the apparent simplicity of these processes, the need to feed the kinetic models with sufficient, pertinent and reliable experimental data on the gas phase and surface reactions has been systematically underlined. At the same time, it has been shown time and again that the deposition mechanisms are considerably complex in the majority of cases. The breakthrough of the present work relies on the modeling of a quaternary system involving complex molecular compounds. By considering the scarcely reported use of CFD calculations for the simulation of film composition, it paves the way to further optimization of state of the art CVD processes and thus shows promise for the use of advanced thin film materials in numerous Key Enabling Technologies. In order to meet this ambitious objective, the next steps in a combined experimental and computational investigation of CVD processes is the consideration of artificial intelligence. Optimization of the exponentially increasing complexity of innovative materials and corresponding fabrication processes could benefit greatly from the data processing acceleration offered through data management, data mining and involved machine learning [43, 44].

Conclusion

The chemical vapor deposition of SiO_xN_y films with non-negligible amount of carbon was executed in the 600-650°C range, utilizing a rarely-investigated silanamine precursor, tris(dimethylsilyl)amine (TDMSA) as a dual silicon and nitrogen source, with O_2 gas as co-

reagent. Given the novelty of the chemistry and the lack of data in the literature, deposition experiments were coupled with gas phase analyses to shed more light into the homogeneous and heterogeneous reactions describing this particular chemical pathway. Recently reported results documenting the gas phase characterization of the SiO_xN_y CVD process were utilized with parallel consideration of solid phase results obtained from spectroscopic ellipsometry (SE) and ion beam analyses (IBA). This combined approach allowed the proposal of an apparent chemical and kinetic model for the deposition of carbonated SiO_xN_y and its application in numerical simulations using computational fluid dynamics (CFD) codes.

The model consisted of eight chemical reactions, with film formation being described via three surface reactions defined by Arrhenius-type kinetic laws and based on the contribution of three intermediate species: a $Me_2SiH°$ radical, a $(Me_2SiH)_2N°$ radical and a fictitious intermediate species N_INT2 of the silanimine family. The deposition process was defined as a simultaneous formation of SiO_2, Si_3N_4 and $Si_3N_4C_{12}$, supposedly homogeneously distributed towards the formation of a global carbonated SiO_xN_y material. Definition of the kinetics of each heterogeneous reaction allowed for the modulation of the resulting film composition in N and C. The model also accounted for the competitive incorporation of N and O by including a homogeneous reaction that reduces the available concentration of nitrogen-containing species in the gas phase when in presence of O_2.

The developed model is valid for low O_2 flow rates (up to 1.2 sccm O_2) and is not only able to predict local deposition rates, but it also provides general estimations of the film composition profiles in Si, O, N and C for a SiO_xN_y material with non-negligible amount of carbon. To the best of the authors' knowledge, this is the first time that a kinetic model is able to represent and quantify the main chemical mechanisms involved in the CVD of a four-component material. This original methodology combining complete experimental gas and solid phase analyses and numerical kinetic modelling could be applied to other CVD processes forming multi-component thin films. Through this novel approach, the compositional analysis of films on complex substrates that are difficult to characterize non-destructively (e.g. hollow bodies, non-line-of-sight geometries, etc.) could be facilitated via CFD simulation. The dissemination of new CVD chemistries towards original applications could also be enhanced.

Acknowledgements

The present work was funded by ANR (Agence Nationale de la Recherche) under the contract HEALTHYGLASS ANR-17-CE08-0056. The authors gratefully acknowledge ANR for supporting the present research. The authors are also thankful to Irea Touche from LGC for her help on the numerical frame and troubleshooting. The authors are indebted to Lionel Rechignat, LCC UPR and Eric Leroy, ICT for fruitful discussions on ESR and GC-MS analyses respectively.

References

[1] M. Shahpanah, S. Mehrabian, M. Abbasi-Firouzjah, B. Shokri, Improving the oxygen barrier properties of PET polymer by radio frequency plasma-polymerized SiO_xN_y thin film, Surf. Coat. Technol. 358 (2019) 91-97. https://doi.org/10.1016/j.surfcoat.2018.11.023.
[2] Z. Zhang, Z. Shao, Y. Luo, P. An, M. Zhang, C. Xu, Hydrophobic, transparent and hard silicon oxynitride coating from perhydropolysilazane, Polym. Int. 64(8) (2015) 971-978. https://doi.org/10.1002/pi.4871.
[3] Y. Shima, H. Hasuyama, T. Kondoh, Y. Imaoka, T. Watari, K. Baba, R. Hatada, Mechanical properties of silicon oxynitride thin films prepared by low energy ion beam assisted deposition, Nucl. Instrum. Methods Phys. Res., Sect. B 148(1-4) (1999) 599-603. https://doi.org/10.1016/S0168-583X(98)00811-8.
[4] E.K. Park, S. Kim, J. Heo, H.J. Kim, Electrical evaluation of crack generation in SiN_x and SiO_xN_y thin-film encapsulation layers for OLED displays, Appl. Surf. Sci. 370 (2016) 126-130. https://doi.org/https://doi.org/10.1016/j.apsusc.2016.02.142.
[5] J. Steffens, M.A. Fazio, D. Cavalcoli, B. Terheiden, Multi-characterization study of interface passivation quality of amorphous sub-stoichiometric silicon oxide and silicon oxynitride layers for photovoltaic applications, Sol. Energy Mater. Sol. Cells 187 (2018) 104-112. https://doi.org/https://doi.org/10.1016/j.solmat.2018.07.024.
[6] B. Hallam, B. Tjahjono, S. Wenham, Effect of PECVD silicon oxynitride film composition on the surface passivation of silicon wafers, Sol. Energy Mater. Sol. Cells 96 (2012) 173-179. https://doi.org/10.1016/j.solmat.2011.09.052.
[7] Y. Shi, L. He, F. Guang, L. Li, Z. Xin, R. Liu, A review: preparation, performance, and applications of silicon oxynitride film, Micromachines 10(8) (2019) 552. https://doi.org/10.3390/mi10080552.
[8] D. Yonekura, K. Fujikawa, R.-I. Murakami, Influence of film structure on gas barrier properties of SiO_xN_y films, Surf. Coat. Technol. 205(1) (2010) 168-173. https://doi.org/https://doi.org/10.1016/j.surfcoat.2010.06.024.
[9] P.-K. Shin, T. Mikolajick, Alkali- and hydrogen ion sensing properties of LPCVD silicon oxynitride thin films, Thin Solid Films 426(1) (2003) 232-237. https://doi.org/https://doi.org/10.1016/S0040-6090(03)00041-5.
[10] D.K.W. Lam, Low temperature plasma chemical vapor deposition of silicon oxynitride thin-film waveguides, Appl. Opt. 23(16) (1984) 2744-2746. https://doi.org/10.1364/AO.23.002744.
[11] W. Gleine, J. Müller, Low-pressure chemical vapor deposition silicon–oxynitride films for integrated optics, Appl. Opt. 31(12) (1992) 2036-2040. https://doi.org/10.1364/AO.31.002036.
[12] B. Kaghouche, F. Mansour, C. Molliet, B. Rousset, P. Temple-Boyer, Investigation on optical and physico-chemical properties of LPCVD SiO_xN_y thin films, Eur. Phys. J.: Appl. Phys. 66(2) (2014) 20301. https://doi.org/10.1051/epjap/2014130550.
[13] Z. Yu, M. Aceves, J. Carrillo, R. López-Estopier, Charge trapping and carrier transport mechanism in silicon-rich silicon oxynitride, Thin Solid Films 515(4) (2006) 2366-2372. https://doi.org/https://doi.org/10.1016/j.tsf.2006.04.009.

[14] E. Halova, S. Alexandrova, A. Szekeres, M. Modreanu, LPCVD-silicon oxynitride films: interface properties, Microelectron. Reliab. 45(5-6) (2005) 982-985. https://doi.org/10.1016/j.microrel.2004.11.011.
[15] L. Decosterd, K.C. Topka, B. Diallo, D. Samelor, H. Vergnes, F. Senocq, B. Caussat, C. Vahlas, M.-J. Menu, An innovative GC-MS, NMR and ESR combined, gas-phase investigation during chemical vapor deposition of silicon oxynitrides films from tris(dimethylsilyl)amine, Phys. Chem. Chem. Phys. 23(17) (2021) 10560-10572. https://doi.org/10.1039/D1CP01129D.
[16] A.M. Wrobel, A. Walkiewicz-Pietrzykowska, I. Blaszczyk-Lezak, Reactivity of organosilicon precursors in remote hydrogen microwave plasma chemical vapor deposition of silicon carbide and silicon carbonitride thin-film coatings, Appl. Organomet. Chem. 24(3) (2010) 201-207. https://doi.org/https://doi.org/10.1002/aoc.1589.
[17] A. Shahmohammadi, R.T. Bonnecaze, Sequential Model-Based Design of Experiments for Development of Mathematical Models for Thin Film Deposition using Chemical Vapor Deposition Process, Chem. Eng. Res. Des. (2020). https://doi.org/10.1016/j.cherd.2020.04.032.
[18] F. Ojeda, A. Castro-García, C. Gómez-Aleixandre, J.M. Albella, Growth kinetics of chemically vapor deposited SiO2 films from silane oxidation, J. Mater. Res. 13(8) (1998) 2308-2314. https://doi.org/10.1557/JMR.1998.0322.
[19] M. Binnewies, K. Jug, The Formation of a Solid from the Reaction SiCl4 (g)+ O2 (g)→ SiO2 (s)+ 2Cl2 (g), Eur. J. Inorg. Chem. 2000(6) (2000) 1127-1138. https://doi.org/10.1002/(SICI)1099-0682(200006)2000:6<1127::AID-EJIC1127>3.0.CO;2-6.
[20] Y. Huang, Modeling and analysis of SiO2 deposition during high-purity fused silica glass synthesis by SiCl4 chemical vapor deposition, Ceram. Int. 45(8) (2019) 10740-10745. https://doi.org/https://doi.org/10.1016/j.ceramint.2019.02.147.
[21] J.P. Nieto, L. Jeannerot, B. Caussat, Modelling of an industrial moving belt chemical vapour deposition reactor forming SiO_2 films, Chem. Eng. Sci. 60(19) (2005) 5331-5340. https://doi.org/10.1016/j.ces.2005.04.079.
[22] D.M. Dobkin, S. Mokhtari, M. Schmidt, A. Pant, L. Robinson, A. Sherman, Mechanisms of Deposition of SiO2 from TEOS and Related Organosilicon Compounds and Ozone, J. Electrochem. Soc. 142(7) (1995) 2332-2340. https://doi.org/10.1149/1.2044296.
[23] S. Ponton, H. Vergnes, D. Samelor, D. Sadowski, C. Vahlas, B. Caussat, Development of a Kinetic Model for the Moderate Temperature Chemical Vapor Deposition of SiO2 Films from Tetraethyl Orthosilicate and Oxygen, Aiche Journal 64(11) (2018) 3958-3966. https://doi.org/10.1002/aic.16222.
[24] K. Yacoubi, C. Azzaro-Pantel, J.P. Couderc, Analysis and Modeling of Low Pressure CVD of Silicon Nitride from a Silane-Ammonia Mixture: II. Deposition Modeling, J. Electrochem. Soc. 146(8) (1999) 3018-3027. https://doi.org/10.1149/1.1392045.
[25] A. Tachibana, K. Yamaguchi, S. Kawauchi, Y. Kurosaki, T. Yamabe, Silyl radical mechanisms for silicon-nitrogen bond formation, J. Am. Chem. Soc. 114(19) (1992) 7504-7507.
[26] D.J. Collins, A.J. Strojwas, D.D. White, A CFD model for the PECVD of silicon nitride, IEEE Transactions on Semiconductor Manufacturing 7(2) (1994) 176-183. https://doi.org/10.1109/66.286853.
[27] K.C. Topka, G.A. Chliavoras, F. Senocq, H. Vergnes, D. Samelor, D. Sadowski, C. Vahlas, B. Caussat, Large temperature range model for the atmospheric pressure chemical vapor deposition of silicon dioxide films on thermosensitive substrates, Chem. Eng. Res. Des. 161 (2020) 146-158. https://doi.org/10.1016/j.cherd.2020.07.007.
[28] B. Diallo, K.C. Topka, M. Puyo, C. Lebesgue, C. Genevois, R. Laloo, D. Samelor, H. Lecoq, M. Allix, H. Vergnes, F. Senocq, P. Florian, V. Sarou-Kanian, T. Sauvage, M.-J. Menu, B. Caussat, V. Turq, C. Vahlas, N. Pellerin, Network hydration, ordering and composition interplay of chemical vapor deposited amorphous silica films from tetraethyl orthosilicate, Journal of Materials Research and Technology 13 (2021) 534-547. https://doi.org/https://doi.org/10.1016/j.jmrt.2021.04.067.
[29] R. Kee, G. Dixon-Lewis, J. Warnatz, M. Coltrin, J. Miller, H. Moffat, A Fortran computer code package for the evaluation of gas-phase, multicomponent transport properties, Report No. SAND86-8246B, Technical Report, Sandia National Laboratories, 1998.
[30] R.G. Xu, Y. Leng, Solvation force simulations in atomic force microscopy, J Chem Phys 140(21) (2014) 214702. https://doi.org/10.1063/1.4879657.

[31] E. Gil, J.B. Park, J.S. Oh, G.Y. Yeom, Characteristics of SiO_x thin films deposited by atmospheric pressure chemical vapor deposition as a function of HMDS/O_2 flow rate, Thin Solid Films 518(22) (2010) 6403-6407. https://doi.org/10.1016/j.tsf.2010.03.170.
[32] J.H. Lee, C.H. Jeong, J.T. Lim, V.A. Zavaleyev, S.J. Kyung, G.Y. Yeom, SiO_xN_y thin film deposited by plasma enhanced chemical vapor deposition at low temperature using HMDS–O_2–NH_3–Ar gas mixtures, Surf. Coat. Technol. 201(9) (2007) 4957-4960. https://doi.org/https://doi.org/10.1016/j.surfcoat.2006.07.075.
[33] S.K. Ray, C.K. Maiti, N.B. Chakrabarti, Low-Temperature deposition of dielectric films by microwave plasma enhanced decomposition of hexamethyldisilazane, J. Electron. Mater. 20(11) (1991) 907-913. https://doi.org/10.1007/BF02816031.
[34] K.C. Topka, Experimental study and kinetic modelling of chemical vapor deposition process of silicon oxide and oxynitride thin films for aqueous corrosion barriers, PhD Thesis, Institut national polytechnique de Toulouse, France, 2021.
[35] J. Henrie, S. Kellis, S.M. Schultz, A. Hawkins, Electronic color charts for dielectric films on silicon, Opt. Express 12(7) (2004) 1464-1469. https://doi.org/10.1364/OPEX.12.001464.
[36] M.E. Coltrin, W.G. Breiland, P. Ho, Model Studies of Chemical Vapor Deposition, Materials Technology 8(11-12) (1993) 250-253. https://doi.org/10.1080/10667857.1993.11784996.
[37] J.-P. Couderc, CVD process engineering : modelling aspects, Journal de Physique IV Proceedings 03(C3) (1993) C3-3-C3-16. https://doi.org/10.1051/jp4:1993301.
[38] C.R. Kleijn, R. Dorsman, K.J. Kuijlaars, M. Okkerse, H. van Santen, Multi-scale modeling of chemical vapor deposition processes for thin film technology, J. Cryst. Growth 303(1) (2007) 362-380. https://doi.org/https://doi.org/10.1016/j.jcrysgro.2006.12.062.
[39] I.G. Aviziotis, T. Duguet, K. Soussi, G. Kokkoris, N. Cheimarios, C. Vahlas, A.G. Boudouvis, Investigation of the kinetics of the chemical vapor deposition of aluminum from dimethylethylamine alane: experiments and computations, physica status solidi c 12(7) (2015) 923-930. https://doi.org/https://doi.org/10.1002/pssc.201510023.
[40] I.G. Aviziotis, T. Duguet, C. Vahlas, A.G. Boudouvis, Combined Macro/Nanoscale Investigation of the Chemical Vapor Deposition of Fe from Fe(CO)5, Advanced Materials Interfaces 4(18) (2017) 1601185. https://doi.org/https://doi.org/10.1002/admi.201601185.
[41] H. Vergnes, D. Samélor, A.N. Gleizes, C. Vahlas, B. Caussat, Local Kinetic Modeling of Aluminum Oxide Metal-Organic CVD From Aluminum Tri-isopropoxide, Chem. Vap. Deposition 17(7-9) (2011) 181-185. https://doi.org/https://doi.org/10.1002/cvde.201004301.
[42] C. Raffy, E. Blanquet, M. Pons, C. Bernard, C. Melius, F., M. Allendorf, D., Contribution to the modeling of CVD silicon carbide growth, J. Phys. IV France 09(PR8) (1999) Pr8-205-Pr8-212. https://doi.org/doi.org/10.1051/jp4:1999825.
[43] K. Alberi, M.B. Nardelli, A. Zakutayev, L. Mitas, S. Curtarolo, A. Jain, M. Fornari, N. Marzari, I. Takeuchi, M.L. Green, M. Kanatzidis, M.F. Toney, S. Butenko, B. Meredig, S. Lany, U. Kattner, A. Davydov, E.S. Toberer, V. Stevanovic, A. Walsh, N.-G. Park, A. Aspuru-Guzik, D.P. Tabor, J. Nelson, J. Murphy, A. Setlur, J. Gregoire, H. Li, R. Xiao, A. Ludwig, L.W. Martin, A.M. Rappe, S.-H. Wei, J. Perkins, The 2019 materials by design roadmap, J. Phys. D: Appl. Phys. 52(1) (2018) 013001. https://doi.org/10.1088/1361-6463/aad926.
[44] Q. Zeng, Y. Gao, K. Guan, J. Liu, Z. Feng, Machine learning and a computational fluid dynamic approach to estimate phase composition of chemical vapor deposition boron carbide, Journal of Advanced Ceramics 10(3) (2021) 537-550. https://doi.org/10.1007/s40145-021-0456-3.